TOWARDS FUNCTIONAL MINIATURIZED LASERS

Thesis by

Zhaoyu Zhang

In Partial Fulfillment of the Requirements for the

Degree of

Doctor of Philosophy

CALIFORNIA INSTITUTE OF TECHNOLOGY

Pasadena, California

2007

(Defended May 3, 2007)

To my parents Kezhao Zhang and Xiaozhou Chen

ACKNOWLEDGEMENTS

My first thanks go to my advisor Axel Scherer, who provided me the opportunity to work in this exciting field and to be a part of his great research group. I would never forget his generosity for having an Aeronautics student trying out the semiconductor laser projects. Needless to say, his tireless efforts have played an important role in the progress I've made the past few years. Beyond this, I have learned immeasurable amounts from him in both science and technology. Moreover, his patience and constant encouragement are what bring me to the stage today.

I also owe a debt of gratitude to my research mentors Dr. David T Wei and Dr. Tomoyuki Yoshie, from whom I learned most of the research techniques on which my work in this thesis is based. From them, I realized the importance of independent research work.

My great thanks also go to my colleagues. This list includes: Dr. Koichi Okamoto, Dr. Terrell Neal, Dr. Lan Yang, Zhenyu Li, Yan Chen, Ting Hong, and David Henry who have been collaborating with me on all my research work thus far; the undergraduate students Julie Sze, Tom Sze, Xiaoliang Zhu, Jiajing Xu, Victor Liu, Jie He, and Geng Wang who helped me on the experimental work in the sweating summers as well as during some of the terms throughout the years; Dr. Haiquan Yang from Epiworks Inc.; Dr. Yueming Qiu from Jet Propulsion Lab; Dr. Yongqin Jiao, Dr. Chi Ma, Dr. George Roseman, Lin Zhu, Dr. Tao Lu, Hong Zhong, Dunwei Wang, Ke Xu, and Xiquan Cui—all from Caltech—who each helped me out in some part of the experiments; Dr. Joyce Wong and Dr. John Choi, who encouraged me all the time and gave valuable advice. Among them, special thanks to Dr.

Koichi Okamoto, Dr. Terrell Neal, Dr. Lan Yang, and Victor Liu, who helped me a lot in many aspects.

Beyond the few I have just named, with whom I have directly interacted the most, I gratefully acknowledge everyone else in the Nanofabrication group, Maladen Barbic, Marko Loncar, Mark Adams, David Barsic, Ali Husain, Jeremy Witzen, Brett Manue, Sven Matthias, Emil Kartalov, Michael Hochberg, Tom Baehr-Jones, George Maltezos, Chris Walker, Teresa Emery, Guangxi Wang, Saurabh Vyawahare, Uday Khankhoje, Michael Shearn, Jingqin Huang, Sameer Walavalkar, and especially our secretary, Kate Finigan, and our lab coordinator, Dr. Guy DeRose, who have been working hard to enable an efficient working environment. I am so lucky to have spent these years with these great people.

Finally, I would like to thank my advisory board: Dr. Axel Scherer, Dr. Amnon Yariv, Dr. Kerry Vahala, Dr. Changhuei Yang, Dr. Marc Bockrath; and the other members in my candidacy committee: Dr. Demetri Psaltis and Dr. Oskar Painter.

ABSTRACT

In this thesis, nanometer scale semiconductor lasers and micrometer scale polymer based dye lasers are our focus in bringing the miniaturized lasers to applications in data transmission; ultra-small chemical / biological sensors; and ultra-compact spectroscopic sources. Combining the advantage of electrically driven semiconductor lasers and the advantage of a broad emission spectrum of dye molecules would utilize the highly dense multi-functional lab-on-a-chip by integrating microfluidic PCR, microfluidic fluorescent detection system, and compact visible and NIR detectors which are commercially available. On the other hand, in the meantime of pushing the size limit of the laser cavities, new phenomena with the nanoscale lasers enable further exploration and understanding in fundamental physics.

In the first part of this thesis, two sub-micron scale semiconductor lasers are presented. The smallest lasers utilizing the disk structures—with diameters of approximately 600 nm—were realized in the InGaP/InGaAlP quantum well material system at room temperature, featuring ultra-small mode volumes of approximately 0.03 μm^3, and exhibiting single-mode operation at low threshold powers. And the first visible photonic crystal ultra-small mode volume lasers, with cavity volumes of approximately 0.01 μm^3, are realized in the same material system. They are ideally suited for use as spectroscopic sources and both of them can be lithographically tuned from 650 – 690 nm.

In the second part of this thesis, two sub-millimeter-scale polymer-based dye lasers—a poly(dimethylsiloxane) (PDMS)-based mechanically tunable DFB dye laser and a

poly(methylmethacrylate) (PMMA)-based second-order circular grating distributed feedback dye laser—are presented. Both of them are compatible with microfluidic technology, which gives freedom in integrating the lasers with the microfluidic chips. Compared to the soft lithography used in the PDMS-based dye laser, the nanoimprint lithography used in the PMMA-based dye laser would be more useful for fabricating ultra-small dye lasers and enabling mass production in the near future.

At the end of the thesis, a nano-linewidth metal grating mask pattern transferred transient grating (MPT-TG) technique is described as a potential technique using the ultra-small lasers for molecular-dynamics study in solutions.

TABLE OF CONTENTS

LIST OF FIGURES

LIST OF TABLES

Chapter 1

INTRODUCTION

In this thesis I am going to introduce two categories of lasers: sub-micrometer-scale cavity semiconductor lasers, and millimeter-scale polymer-based dye lasers. In the first category, I will talk about two kinds of ultra-small cavity designs. The first is the submicron microdisk cavity and the second is the photonic crystal defect cavity. In the second category, I am going to talk about: the microfluidic one-dimensional DFB dye laser, and the solid-state two-dimensional circular grating DFB dye laser, with a focus on the potiential application on the micro optofluidic "lab-on-a-chip". In the end, I will talk about how we can apply these lasers to the build a lab-on-a-chip by developing a technique for the molecular dynamic study in the solution.

1.1 Background and motivation

As does all matter exhibiting the wave-particle duality, light or electromagnetic radiation simultaneously exhibits properties of both waves and particles. In the scope of our research, both properties are substantial. The elementary particle that defines the light is the photon. There are many means of photon generation (many sources of light). In the semiconductor material we are working on, photons are produced through the energy transferred by either external photon pumping or the recombination of electron-hole pairs. In the dye materials, the photons are generated by external photon pumping only. Of the three macroscopic properties of light (photons)—intensity, frequency, and polarization—we will mainly focus

on the property of frequency, and we will mainly work on how to control the light within a small space, and together with gain material, how to form a laser, a “single-frequency” light source. In physics, a laser is a device that emits light through a specific mechanism for which the term “laser” is an acronym: Light Amplification by Stimulated Emission of Radiation. In contrast to a light source such as the incandescent light bulb, which emits in almost all directions and over a wide spectrum of wavelength, laser emits light with a well-defined wavelength (or color, normally in levels from submicron to tens of microns) and normally in a narrow and well-defined beam. These properties can be summarized in the term “coherence”, and these properties have made lasers a multi-billion dollar industry. The most widespread use of lasers is in optical storage devices such as compact disc and DVD players, bar-code readers, and laser pointers. In industry, lasers are used for cutting steel and other metals, and for inscribing patterns (such as the letters on computer keyboards). Lasers are also commonly used in various fields in science (especially spectroscopy), typically because of their well-defined wavelength or short pulse duration (in the case of pulsed lasers). Most importantly, lasers are also used in optical integrated circuits for optical telecommunication, as well as in biological, chemical, and medical applications.

For the first category of laser, we are trying to explore the limit of the miniaturization of laser cavities and to develop nanophotonic lasers (microdisk and photonic crystal lasers) for applications including use in chip scale optical networks, ultra-small optical spectroscopy, and biological and chemical sensors. The nanolasers will be efficient and compact multi-wavelength light sources with greater density and modulation speed (over 100 Gb/s) than vertical cavity surface emitting lasers. Fast detectors for light have already been developed

in well-established silicon CMOS processes for sensitive receivers, and these lasers can provide optical solutions to the interconnect problems for the next generation of high-speed processors and aerospace platforms. Moreover, it will be possible to assemble these devices into complex systems that permit signal processing and optical logic functions before signal conversion from the optical into the electrical domain.

For the second category of lasers, we are trying to revisit the dye laser, but with a focus on low cost and reusability based on the silicone elastomer process technology and nanoimprint technology. Besides the advantage of the wide emission spectrum of the dye itself, in which the pico-second or even the femto-second lasers could be realized, these lasers are expected to be fully compatible with the current soft-lithographical-defined microfluidic devices. Due to the elastic properties of the skeletal material, they have the unique property of being mechanically tunable. The implementation of these millimeter-scale dye lasers on a microfluidic chip would be very important for making fully functional "lab-on-a-chip" systems for very important applications such as fluorescent analysis in biological and chemical analysis.

1.2 Organization of the thesis

Chapter 2 describes the general fabrication process and laser characteristic measurement setups of the semiconductor nanolasers and the organic dye lasers. This chapter compares the different fabrication techniques, as well as the different equipment available, and gives the practical guidelines for making our nano-scale laser devices. Several important techniques, such as wafer design and epitaxy growth, electron beam lithography, reactive

ion beam etching, inductively coupled plasma etching, and membrane formation are described in detail.

Chapter 3 describes the performance of submicron microdisk lasers fabricated within InGaP/InGaAlP quantum well material working at room temperature. The smallest lasers, with diameters of approximately 600 nm, feature ultra-small mode volumes and exhibit single-mode operation at low threshold powers. Their small cavity volumes of approximately 0.03 μm^3 enable microdisk lasers to be used as spectroscopic sources. In this chapter, we demonstrate the fabrication and characterization of visible, monolithically fabricated, submicron microdisk lasers. Also, we demonstrate refractive index monitoring by using these ultra-small lasers, and compare the results with that of photonic crystal lasers.

Chapter 4 describes the fabrication and performance of photonic crystal lasers fabricated within thin membranes of InGaP/InGaAlP quantum well material and emitting in the visible wavelength range. These lasers have ultra-small mode volumes, emit red light, and exhibit low threshold powers. They can be lithographically tuned from 650 – 690 nm. Their cavity volumes of approximately 0.01 μm^3 are ideally suited for use as spectroscopic sources.

In Chapter 5, single-frequency lasing from organic dye solutions on a monolithic poly(dimethylsiloxane) (PDMS) elastomer chip is demonstrated. The laser cavity consists of a single mode liquid core/PDMS cladding channel waveguide, and a phase-shifted 15th order distributed feedback (DFB) structure. 1 mM solution of Rhodamine 6G in a methanol

and ethylene glycol mixture was used as the gain medium. Using 6 nanosecond 532 nm Nd:YAG laser pulses as the pump light, we achieved threshold pump fluence of ~0.8 mJ/cm^2 and single-mode operation at pump levels up to ten times the threshold. This microfabricated dye laser provides a compact and inexpensive coherent light source for microfluidics and integrated optics covering the spectral region from near-UV to near-IR.

In Chapter 6, a continuously tunable optofluidic distributed feedback (DFB) dye laser is demonstrated on a monolithic poly(dimethylsiloxane) (PDMS) chip. The optical feedback was provided by a phase-shifted higher order Bragg grating embedded in the liquid core of a single-mode buried channel waveguide. Due to the elastomer nature of PDMS, the tunable output was obtained by mechanically varying the grating period. Nearly 60 nm tuning range from a single chip was achieved with two dye molecules: Rhodamine 6G and Rhodamine 101. Single-mode operation was maintained with less than 0.1 nm linewidth. Because of the higher-order grating, a single laser, when operated with different dye solutions, can provide tunable output covering from near-UV to near-IR spectral region. An array of five DFB dye lasers with different grating periods was also demonstrated on a chip. Such tunable integrated laser arrays are key components in advanced spectroscopy.

Chapter 7 demonstrates an optically pumped, surface emitting, polymer dye laser fabricated by nanoimprint lithography. Our laser is based on an organic dye hosted within a poly(methylmethacrylate) matrix coated on a transparent substrate, and the laser cavity consists of a second-order circular grating distributed feedback structure. Using 6 nanosecond 532 nm Nd:YAG optical pump pulses, laser emission peaked at 618 nm with a

linewidth of 0.18 nm and a threshold of 1.31 nJ/mm^2. The nanoimprinted solid-state dye laser geometry described here offers a low cost and compact coherent light source for lab-on-chip spectroscopy systems, a low pump threshold, and geometry well matched to a light emitting diode (LED) pump source. LED-pumped nanoimprinted dye lasers provide an interesting alternative for high-power and portable polymer laser devices.

Chapter 8 describes a mask pattern transferred transient grating (MPT-TG) technique by using metal grating films. Transient thermal grating is generated by an ultraviolet light pattern transfer to nitrobenzene in 2-propanol solution, and the subsequent effect is detected through its diffraction to a probe beam. The thermal diffusion coefficient is obtained by the relationship between the grating periods and the signal decay lifetime, and is well in agreement with the calculated value. This technique has many advantages, such as a simple setting, an easy alignment, accurate phase control, and high stability for molecular-dynamics study in solutions.

Chapter 2

FABRICATION PROCEDURE AND TESTING SETUP

2.1 Introduction

In this chapter, the fabrication procedures and the testing setups for the sub-micrometer lasers, the submicron disk laser and the photonic crystal laser are detailed. The fabrication and testing setups for the dye lasers are described in the corresponding chapters later on.

2.2 Wafer design and epitaxy growth

Our group has been working on the III-V epitaxy light emitting materials which could be grown by metalorganic vapour phase epitaxy (MOCVD), liquid phase epitaxy (LPE), and molecular beam epitaxy (MBE). Epitaxy describes an ordered crystalline growth on a monocrystalline substrate. Different from other thin-film deposition methods, such as thermal evaporation or ion sputter deposition which deposit polycrystalline or amorphous films even on single-crystal substrates, in epitaxy growth the deposited film takes on a lattice structure and orientation identical to those of the substrate. In other words, the substrate acts as a seed crystal. Previously, in our group, we mainly focused on the InGaAsP quantum well material system (Table 2.1) and InAs quantum dots within the InGaAs material (Table 2.2). Both of them emit light in the near infrared spectrum for the application of telecommunication. In this thesis, we will focus on the visible emission materials InGaP/InGaAlP quantum well material system (Table 2.3).

Materials	Function	comments	doping [1/cm^3]	thickness(nm)
p-InP	cap		1.00E+17	50
p-InGaAsP	carrier confinement		1.00E+17	97
i-InGaAsP	carrier confinement		undoped	20
i-InGaAsP	QW	.85%compressive strain	undoped	9
i-InGaAsP	barrier		undoped	20
i-InGaAsP	QW	.85%compressive strain	undoped	9
i-InGaAsP	barrier		undoped	20
i-InGaAsP	QW	.85%compressive strain	undoped	9
i-InGaAsP	barrier		undoped	20
i-InGaAsP	QW	.85%compressive strain	undoped	9
i-InGaAsP	carrier confinement		undoped	20
n-InGaAsP	carrier confinement		1.00E+17	97
n-InP	sacrificial layer		3e+18 ->1e+17	300
n-InP	sacrificial layer		3.00E+18	1200
n-InGaAs	etch stop		3.00E+18	20
n-InP	buffer		3.00E+18	400
n-InP	substrate			

Table 2.1 Layer structures of InGaAsP quantum well samples for infrared photonic crystal lasers

Material	Function	Doping [cm^{-3}]	Thickness [nm]	QD Density [$/cm^2 \cdot$layer]
p-GaAs:Be	cap layer	4×10^{17}	10	
p-$Al_{0.16}Ga_{0.84}As$:Be	carrier confinement	4×10^{17}	25	
i-GaAs	barrier	undoped	25	
i-InAs QDs	Active region	undoped	5	1×10^{10}
i-GaAs	barrier	undoped	25	
i-InAs QDs	Active region	undoped	5	1×10^{10}
i-GaAs	barrier	undoped	25	
i-InAs QDs	Active region	undoped	5	1×10^{10}
i-GaAs	barrier	undoped	25	
i-InAs QDs	Active region	undoped	5	1×10^{10}
i-GaAs	barrier	undoped	25	
i-InAs QDs	Active region	undoped	5	1×10^{10}
i-GaAs	barrier	undoped	25	
n-$Al_{0.16}Ga_{0.84}As$:Si	carrier confinement	1×10^{17}	25	
n-GaAs:Si	-	1×10^{17}	10	
n-$Al_{0.94}Ga_{0.06}As$:Si	sacrificial layer	1×10^{18}	800	
n-GaAs	substrate	1×10^{18}		

Table 2.2 Layer structures of InAs/InGaAs quantum dot samples for infrared low-threshold photonic crystal lasers (courtesy of Yoshie)

In Tables 2.1 and 2.2, the p, i, and n in front of the material indicates the doping type: p-

Material	Layer Name	Target Thickness @ Center (nm)	Type	Target Concentration @ Center (cm-3)
InGaP	Cap	10	N	2E17
{Al(x)Ga}InP	Clad	58	N	2E17
{Al(x)Ga}InP	Barrier	10	u.d.	-
InGa(x)P	2x Well	7	u.d.	-
{Al(x)Ga}InP	2x Barrier	10	u.d.	-
{Al(x)Ga}InP	Clad	58	N	2E17
InGaP		10	N	2E17
Al(x)GaAs		700	u.d.	-
GaAs	Buffer	100	u.d.	-
GaAs	Substrate		SI	

Table 2.3 Layer structures of InGaP/InGaAlP quantum well samples for visible photonic crystal lasers and submicron disk lasers

type, intrinsic, and n-type. Normally, we use Zn for the p-type, and Si for the n-type doping. For the optically pumped lasers, it doesn't necessary to put doping. However, the doping wafer would expect to have high carrier density. A cap layer is often put on top of the slab layer for protection from oxidation in case an aluminum component is present. At the end of the fabrication procedure, the cap layer would be removed by chemical wet etching, leaving the slab layer intact. The slab layer, also called the active layer, normally consists of cladding, quantum well (quantum dot), and barrier layers. Quantum well (quantum dot) layers are designed to match the wavelength range we expect. In the case of Table 2.1, the quantum wells are formed by different composition of the quaternary InGaAsP compound layer to emit light around 1550 nm. In the case of Table 2.2, the quantum dots are formed by InAs and GaAs lattice mismatch layers to emit light around 1300 nm. In the scope of

this thesis, the quantum wells are formed by a ternary InGaP compound layer and a quaternary InGaAlP compound layer to emit light around the 670 nm. Due to the different emission wavelength, the thickness of the slab layer is designed to be 330 nm, 245 nm, and 170 nm in order to contain only the fundamental mode in the vertical direction. Underneath the quantum wells, a 700 nm–1000 nm sacrificial layer was grown. This would be removed to form a two-dimensional membrane structure with large contrast in the refractive index to tightly confine in the vertical direction. The thickness of this layer prevented the leakage of the light into the substrate. The symmetric structure would ensure the high quality-factor resonator design. A buffer layer was usually applied in order to have the lattice match to the quantum well system we needed. Note that we tried to avoid doping in the quantum wells due to degradation of the quantum efficiency by the dopants. However, due to the thin cladding layer (58 nm–110 nm), the concentration of dopants in the cladding can't be very high in order to keep the quantum wells intact by diffusion during the wafer growth. In the wafer design for the electrically driven photonic crystal laser, the doping would be very crucial. The metal contact put on the device would require high doping concentration for the formation of the ohmic contacts. On the other hand, the thin cladding layer would make it very difficult to prevent metal diffusion into the quantum wells, especially when high annealing temperature and long annealing time are required to form the ohmic contact. To solve this problem, we came up with the design shown in Table 2.4.

In this design, we put 200 nm GaAs lattice matched cap layer on top of InGaP cap layer for the purpose of the contact. Since the doping for n-type is still lower than that in p-type in this material system, we still put the p-type on top and the n-type on the bottom of the slab

layer. In this way, the carriers in the devices were limited by the p-type area most. The gradient doping concentration was applied here with higher concentration away from the

Material	Function	Target Thickness @ Center (nm)	Type	Target Concentration @ Center (cm-3)
GaAs	Cap	200	P	5E19 (for contact)
InGaP	Cap	10	P	8E17
{Al(x)Ga}InP	Clad	58	P	-
{Al(x)Ga}InP	Barrier	10	u.d.	-
InGa(x)P	2x Well	7	u.d.	-
{Al(x)Ga}InP	2x Barrier	10	u.d.	-
{Al(x)Ga}InP	Clad	58	N	1E17
InGaP		10	N	5E17
Al(x)GaAs		700	N	1E18
GaAs	Buffer	100	N	2E18
GaAs	Substrate		N+	2E18 or higher (for contact)

Table 2.4 Layer structures of InGaP/InGaAlP quantum well samples for electrically driven visible photonic crystal lasers and submicron disk lasers

quantum wells. We also left the top cladding without doping, since the dopant we used for p-type is znic and it has very high diffusion coefficient. This way, we created a diffusion buffer that allows the zinc diffusion for a certain amount of length. The top layer was doped with carbon which couldn't be doped high enough in the InGaP and InGaAlP layers but GaAs. This layer was designed to dope to $10^{19}/cm^3$. The contact testing with Pt/Ti showed the excellent ohmic contacts.

2.3 Fabrication procedures

In the last section, the design of epitaxial layers for wafer growth was described. In the following sections, some other typical semiconductor fabrication technologies for creating the nano-scale lasers are presented. They include oxide film formation using PECVD, photolithography and electron beam (EB) lithography, dry etching and wet etching. We use these technologies in different steps of our fabrication procedures. And for different devices, they are slightly different which we will describe in detail in the later chapters. Here I would like to give an overview of these technologies. Why do we choose these technologies and what are the important parameters we need to pay much attention when we fabricate the devices? All the steps are important for the results. However, some are repeatable and stable while others are not.

- PECVD oxide growth

PECVD oxide growth is the one which is repeatable and the properties are stable with time and in most of the chemicals. This oxide layer was used for the hard mask of the dry etching. So the requirement of this layer is first keeping the composition of the oxide the same, and second keeping the density the same. The actual components in this layer are the mixture of Si_xO_y and Si_xN_y. By keeping the same recipe, we have had no difficulty in maintaining the same quality of this hardmask layer. For the RF power, the chamber pressure was set to 22W and 900 mtorr. The flow rate of SiH_4 and N_2O gases was set to 100 and 300 sccm, respectively. This PECVD silicon oxinitride growth recipe would give a deposition rate of about 25 nm/sec. There's another option of using Spin On Glass (SOG)

as an etch mask, instead of PECVD oxide. However, due to the stress induced by the thermal process, SOG has the possibility of cracking, and the etching rate is much slower than the PECVD oxide.

- Electron beam lithography

Other than PECVD oxide growth and wafer growth, these steps are falling into two categories: pattern defining (electron beam lithography and photolithography) and pattern transferring (dry etching, which includes reactive ion etching and inductive coupled plasma etching or chemical assist ion beam etching). Due to the small feature size of our devices (e.g., 100 nm hole size), tens of nanometers of resolution in fabrication is required.

Typical lithograph methods that could satisfy this requirement are limited to electron beam lithography and industrial photolithography technology, such as deep ultraviolet lithography, which uses KrF or ArF light sources due to the shorter wavelength. Although the latter has the advantage of fast speed and mass production, but the resolution is thus far still limited by the wavelength of the light. Focus ion beam system is sometimes used for small feature device fabrication. However, due to the high-energy ion bombardment, the surface of the devices which are exposed to the ion beam would have the problem of ion damage. For the light emitter devices we are working on, this would be very risky thing to do. In this thesis work, Leica EBPG 5000 EB lithography system has been used to define the patterns in the EB resist. Compared to the conventional EB system which was converted by scanning electron microscopy, this system has the advantages of fast speed and much larger area writing. Previously, in our group, we used the converted Hitachi S-

4500 system for EB lithography. The comparison of the parameters we normally use of these two systems is shown in Table 2.5 (courtesy of Yoshie). For the limit condition, the resolution of EBPG is less than 1 nm while the Hitachi is about 1 nm.

A proper selection of the electron beam resist is very crucial to obtain the resolution inherent to the EB lithography systems. Three types of electron beam resists were used in this thesis work: 950 K molecular weight single layer PMMA resist, ZEP520 resist, and

System	Electron Gun	V_{acc}	Beam Spot	Current
1) Hitachi S-4500	Cold Field Emission	30 kV	1 nm	50 pA
2) Leica EBPG 5000	Thermal Field Emission	100 kV	30 nm	1 nA

Table 2.5 Electron beam lithography systems used in our group. V_{acc} is the acceleration voltage. (courtesy of Yoshie)

950K/495 K bilayer PMMA resists. PMMA is an abbreviation for poly-methylmethacrylate. Both PMMA and ZEP are positive resists for high-resolution lithography. Figure 2.1 and Figure 2.2 show the scanning electron micrographs of samples after EB lithography with under exposure (lower dose) and right exposure (correct dose) respectively. ZEP520 resist was electron beam written with photonic crystal pattern and developed by amyl acetate. The bilayer PMMA resist are used when a lift-off process is needed. As for the chemical resistance, although ZEP520 resist is not as good as the photoresists, it is much better than PMMA and almost all other electron beam resists. For example, etching rate of ZEP520 in CHF_3 reactive ion etching is less than 5 nm/minute while about 40nm / minute for 950K PMMA. Hence, the selectivity of ZEP over SiON is

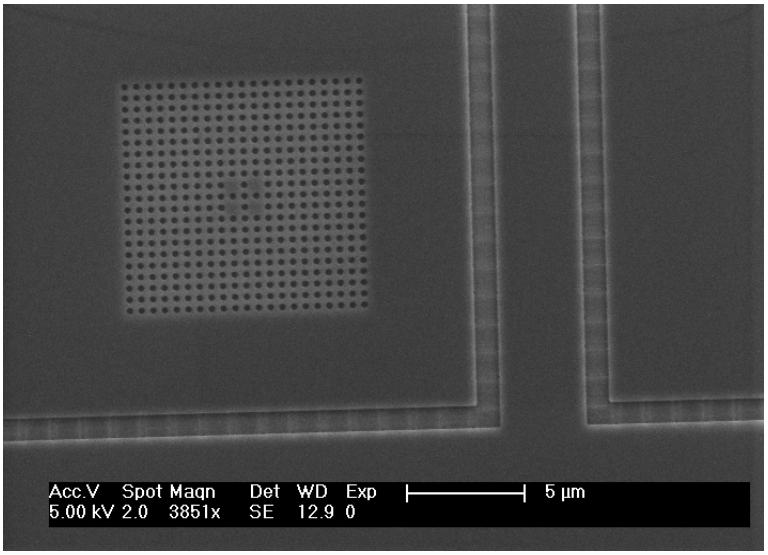

Figure 2.1 This top-view SEM micrography shows the developed ZEP profile after EBPG electron beam writing with low beam dose. The underexposed condition could be clearly seen from the strips in the 1 micron trench area.

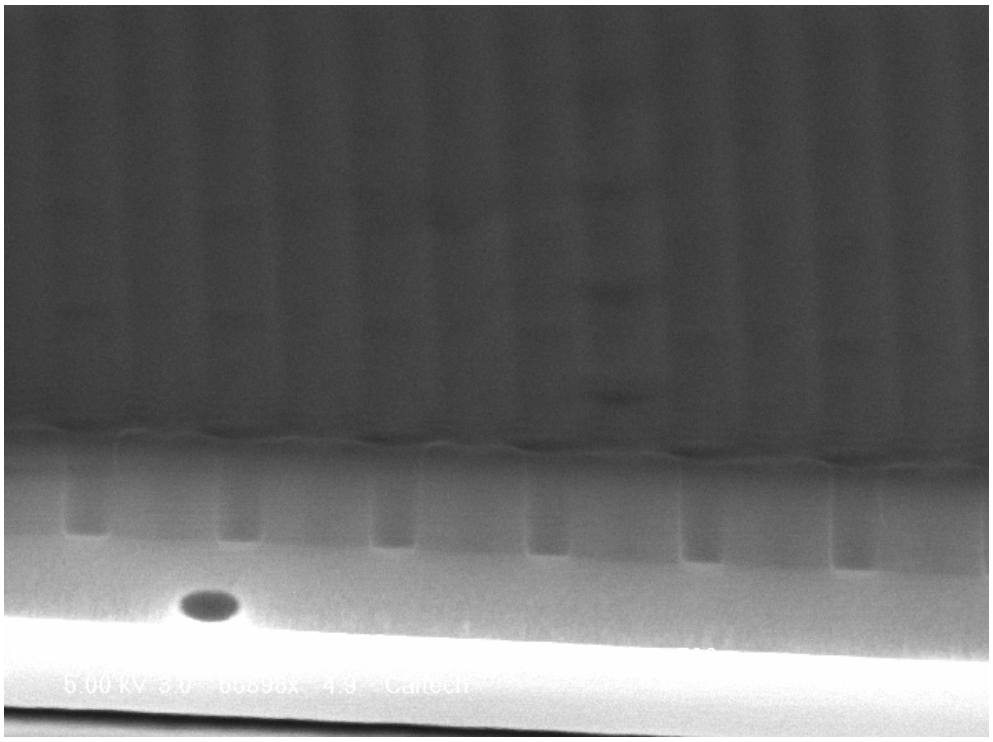

Figure 2.2 Developed ZEP profile after EBPG electron beam writing with correct dose. The hole profiles in the ZEP layer are very good. The black circle is a bubble in the SOG layer. The substrate in this photo is GaAs based InGaP/InGaAlP quantum well system. This sample was cleaved in order to show the cross-section features.

much less than PMMA over SiON (which is about 1:1 in this chemistry). This good selectivity gives us more chance to get good pattern transferring from the resist into the hardmask SiON layer. On the other hand, good chemical resistance causes problems when the resist needs to be removed. Fortunately, like many other polymers, ZEP520 decomposes when irradiated by deep ultraviolet light. In practice, a 254 nm ultraviolet light was used to irradiate the samples for about half an hour. Then 90°C hot n-methylpyrrolidone (NMP) was used to dissolve the decomposed ZEP520 resist.

- Reactive ion etching of SiON hardmask

After the EB lithography, the defined patterns were transferred into the hard etch mask layer or the substrates using the dry etching techniques. Since the quantum well layers would be exposed to the etching environment, the etching methods are required to do less damage to these layers besides the precise transferring of the pattern into the dielectric materials, such as InGaAsP or InGaP/InGaAlP. Here, four types of etching are present, depending on the material we etch.

For etching SiON hardmask, we used reactive ion etching (RIE). Compared to the barrel etcher, the RIE employs capacitively coupled plasma and provides good directional etching or anisotropic etching. Trifluoromethane (CHF_3) chemistry was used to etch the SiON layer and ZEP520 was used as an etching mask due to the good selectivity over the SiON in CHF_3 chemistry as mentioned above. The good result was obtained in our system when using 20 sccm flow rate of CHF_3, 16 mTorr of chamber pressure, 90 W of RF power, and 3 inches parallel plate distance. The DC bias was typically around 500 V and the

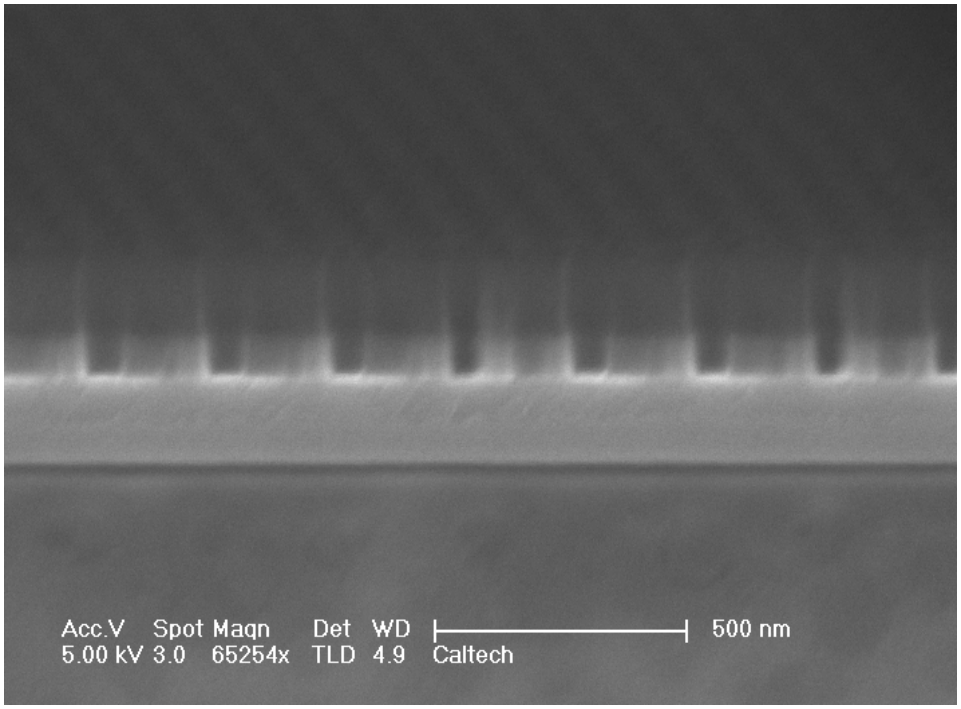

Figure 2.3 SEM micrographs of a reactive ion etching result. The CHF_3 plasma transfers the patterns in ZEP520 into the SiON etch mask. Note that the hole size in the picture is less than 100 nm.

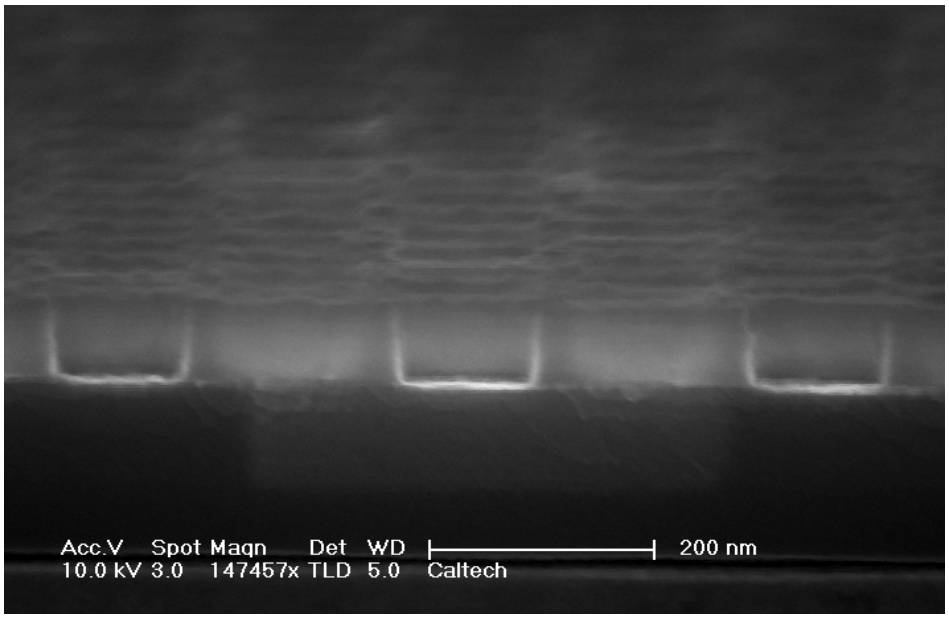

Figure 2.4 SEM image of the cross section of a ZEP removed sample with photonic crystal pattern in the 100 nm thick SiON. The roughness on the top surface may be the leftover ZEP resist which we removed using the descum in ICP.

etching rate was around 40nm/minute. Figure 2.3 shows an SEM image of a cleaved sample cross section after the CHF_3 RIE etching. After etching, the ZEP resist was removed by 254 nm deep UV exposure followed by chemical dissolution in order to have a clean etched mask for the next inductively coupled plasma (ICP) etch. Figure 3.4 shows the SEM image of the same chip after the removal of the resist.

- Inductively coupled plasma relative ion etching (ICPRIE)

The inductively driven source at 13.56MHz provides good discharge efficiency because only a small part of the voltage is dropped across the plasma sheath, which is a thin positively charged layer, and the loss of ion energy is much smaller than in capacitive coupling. Compared to RIE process, the ICPRIE has the freedom to control the plasma density and ion energy separately. Thus, the control of physical ion bombardment and chemical reaction could be more independent. Therefore, ICP-RIE etch technique could produce high aspect ratio structure without large damage to the surface of the materials.

We used hydrogen iodine (HI) and chlorine mixture for our ICP RIE etching of InGaAsP and InGaP/ InGaAlP systems. HI has the advantage of smooth etching surface and it reacts with the indium component at room temperature, while chlorine chemistry leaves $InCl_3$ reaction product which can only be removed at $150^{o}C$ or higher temperatures. On the other hand, chlorine is a very active gas for etching the GaAs matierals. The mixture of these two gases was optimized to have a better etching result for different materials. Figure 2.5 shows the InGaAsP etching result under the condition of 20 sccm, 9 sccm, 5 sccm of HI, H_2 Cl_2 flowrates respectively, 10 mTorr chamber pressure, 850 W of ICP power, and 100 W of RF

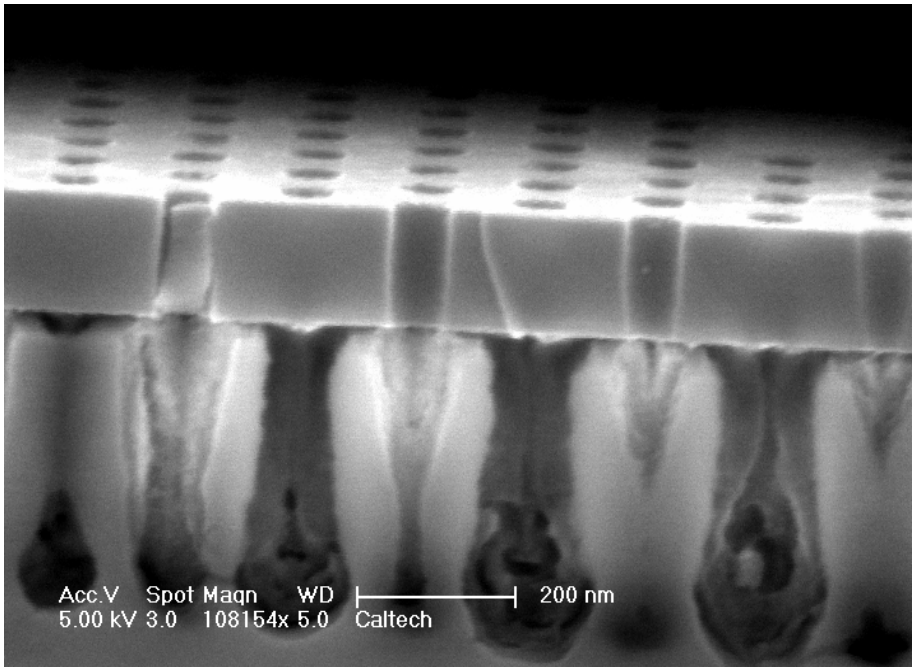

Figure 2.5 The hole profiles on the QW layer after ICP-RIE. The SiON and ZEP layers are removed. The black and white irregular shape area underneath the slab layer is due to the oxidation of AlGaAs in the air.

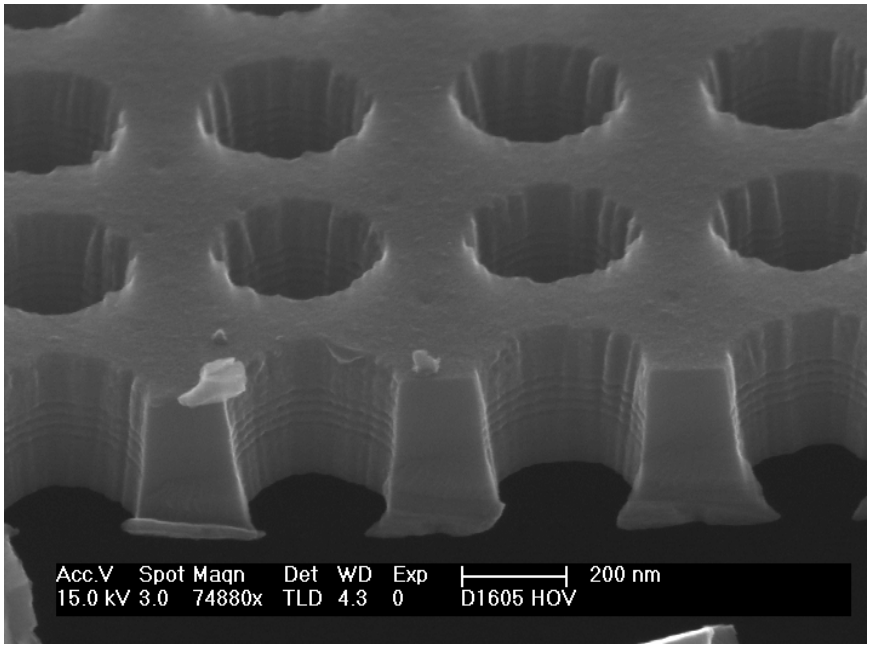

Figure 2.6 The hole profiles on the InGaAsP QW layer after ICP-RIE and chemical undercut. The inclined the sidewall was due to the short time etching of the sample. And on the image, the quantum wells are clearly seen due to the slightly chemical etching.

power. Figure 2.6 shows the InGaP/ InGaAlP etching result under the condition of 20 sccm, 10 sccm, 7 sccm of HI, H_2 Cl_2 flowrates respectively, 10 mTorr chamber pressure, 300 W of ICP power, and 100 W of RF power.

- Undercut and drying process

After the ICP RIE etching, samples were undercut and the SiON mask layers were removed using buffered hydrofluoric acid (HF). For the InGaAsP material system, the InP sacrificial layer was partially removed by diluted hydrochloric acid (HCl). For InGaP/InGaAlP material system, normally we thermal oxidized the AlGaAs sacrificial layer and then Al_xO_y was removed by potassium hydroxide (KOH). The exposure time to the air between the ICP-RIE etching and thermal oxidation is very crucial, due to the easy oxidation in the air (with water vapor in presence) of our AlGaAs sacrificial layer which has Al of 95% in the composition. The sample drying process in the end is also very important in forming symmetric slab (membrane) structures. Trapped liquid underneath the membranes pulls it down during the evaporation process due to the surface tension. This would result in bent membranes or even broken structures. In our process, we typically apply hexane or isopropyl alcohol as the last rinsing solvent because of their low surface tension. A safer way to prevent the bending of the membrane is critical point drying, in which the solvent is replaced by carbon dioxide (CO_2) liquid, due to the low critical point of CO_2. And then the temperature and pressure are increased until the solution is supercritical and the liquid changes to gas without damaging the sample.

- Photolithography and lift off

Photolithography here was used for defining the metal contact patterns for electrically pumped devices and it doesn't require as high resolution as electron beam lithography. However, sometimes, the bilayer photoresist, such as Shipley SH1812 and Shipley LOR were used together to get good lift off results.

2.4 Measurement setups

In this section, we will briefly describe the measurement setups for the laser characterization for our nano-scale lasers. All of them are micro photoluminescent setup. First is a horizontal configuration, which is better for reconstruction and good for adjusting the focal length (Figure 2.7). The second one is a vertical configuration, which is good for measuring signals from the samples in solution; also it has the advantage of easy mounting of the sample by simply placing the chip onto the stage (Figure 2.8). The third setup is for the measurement of the electrically driven devices (Figure 2.9), which incorporates the probe stations as well as the semiconductor parameter analyzer for measuring the relation between the driving current of the devices and voltage across them. Since this setup was directly built up from a vertical stereo microscope system, the magnification can be changed (rotating the objectives) without adjusting the sample's working distance. The first and the second setups are typical optical micro-photoluminescent measurement setup while the third is built to meet the need to measure electrical properties with optical properties simultaneously in the micro, nano-scale devices.

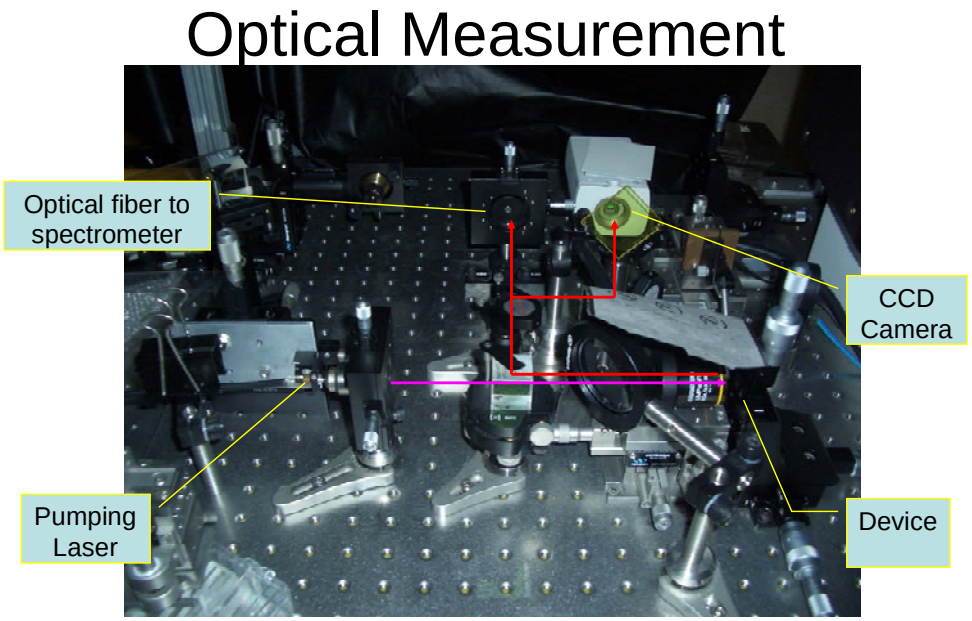

Figure 2.7. Horizontal setup for optical pumping of nanolasers. The pumping diode laser path is shown in thick line. It passes through an objective. Emissions from the sample are sent back through the same objective and through a beam splitter. The thin line path shows two possible destinations, the CCD camera to help align the sample, and the optical fiber coupled to the spectrometer.

Figure 2.8. Vertical setup for optical pumping of nanolasers. It is similar to the horizontal setup but the pumping diode laser is on top and the sample stage is placed on the optical table on the bottom. The pump light also passes through a microscope objective. Emissions from the sample are sent back through the same objective and through a splitting prism. The CCD camera is to help alignment of the sample, and the optical fiber is coupled to the spectrometer

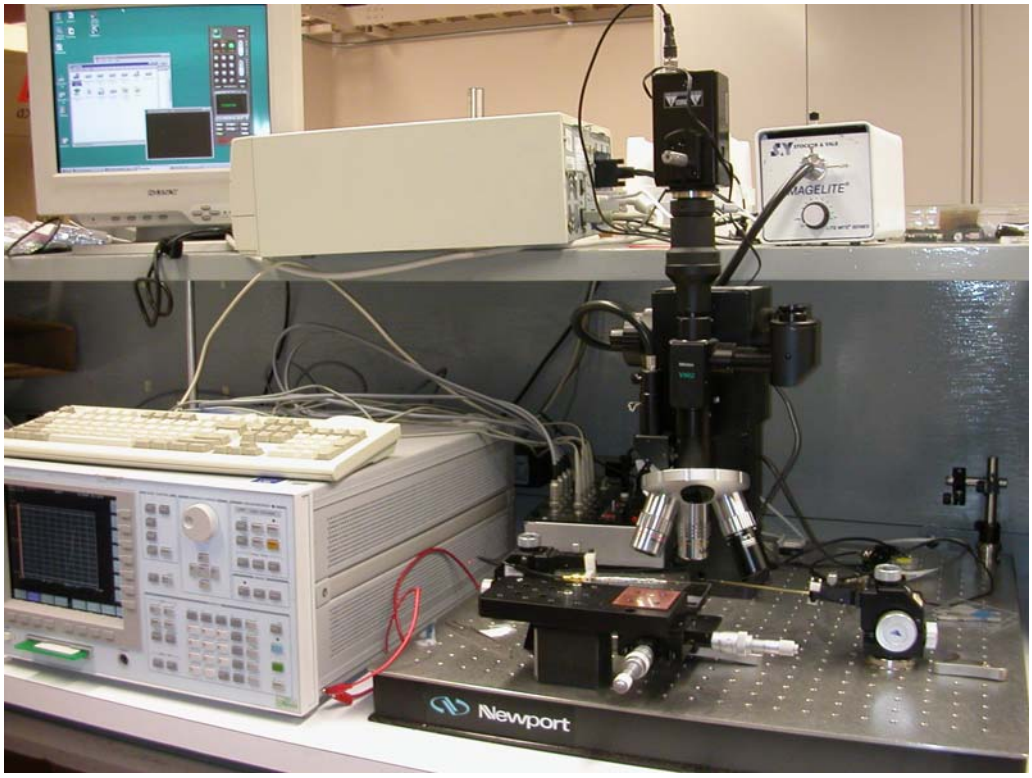

Figure 2.9. Vertical setup for electrical pump of nanolasers. The semiconductor parameter analyzer is used to characterize the metal contact as well as the device diode property. In the meanwhile, it pumps the device. The emission was collected by a stereo microscope with CCD. Three different magnification objectives enable the device alignment. The optical fiber is coupled to the cooled CCD spectrometer.

Chapter 3

VISIBLE SUB-MICROMETER MICRODISK LASERS

3.1 Introduction

Semiconductor microdisk lasers based on micro-fabricated whispering gallery mode cavities have been studied for over 15 years, and were originally pioneered in InGaAsP material emitting in the near-infrared telecommunication wavelength range, as this material exhibits low surface recombination losses. High Q-factors, monolithic fabrication, and the possibility of dense integration make the microdisk geometry a very promising candidate for optical communications and chemical sensing. By selecting various material systems, microdisk lasers have been demonstrated at many different wavelengths ranging from the UV to the IR [1-6]. By depositing one contact on the top surface of the disk and establishing a conducting path from the laser through the substrate, electrical injection lasers have also been realized in this geometry [7-9]. Shrinking the disk size was shown to enable large-scale integration and low energy consumption. However, due to the high optical bend losses inherent to small disk microcavities, much research still focuses on cavity sizes over 2 μm in diameter. The smallest disk laser reported in the literature so far consisted of a 1.6 μm diameter "thumbtack" laser fabricated in the InGaAs/InGaAsP quantum well (QW) material system, emitting light at wavelength of 1.54 μm in 1993 [10].

In this chapter, we report even smaller visible microdisk lasers fabricated in InGaP/InGaAlP QW material and emitting light at a wavelength of approximately 645 nm.

The 645±5 nm diameter of our free-standing disk laser is about the same as the vacuum emission wavelength. To our knowledge the diameter relative to the wavelength is even smaller than previous reported results. Furthermore, the device operates at room temperature with a low excitation threshold of 50 μW. The cavity volumes of these laser devices, calculated to be approximately 0.03 μm^3, are well suited for the exploration of laser performance at the extreme limits of laser size. Ultra-small lasers in visible light emitting material systems are also expected to be excellent spectroscopy sources to perform very local chemical and biological measurements.

3.2 Ultra-small microdisk lasers

InGaP/InGaAlP quantum wells were grown by metal-organic chemical-vapor deposition (MOCVD) on top of a sacrificial AlGaAs layer, deposited onto a GaAs substrate. Optical gain was provided by two 7 nm thick and compressively strained InGaP quantum wells that were separated by 10 nm InGaAlP barriers (Figure 3.1 (a)). The active quaternary material was designed to emit light at ~670 nm (Figure 3.1 (b)). Due to the compressively strained quantum wells, light was strongly coupled into transverse electric (TE) modes. The quantum well active material was placed within the center of a 170 nm InGaAlP slab, and 10 nm InGaP lattice matched layers were used on the top and bottom sides of the slab to prevent the oxidation of aluminum in the quaternary compound. A 700 nm thick sacrificial AlGaAs layer was introduced between the slab and the GaAs substrate, designed to be removed through a selective chemical etch to avoid coupling losses from the disk wings into the substrate. Following epitaxial growth of the InGaP/InGaAlP material, the wafers were coated with a 100 nm

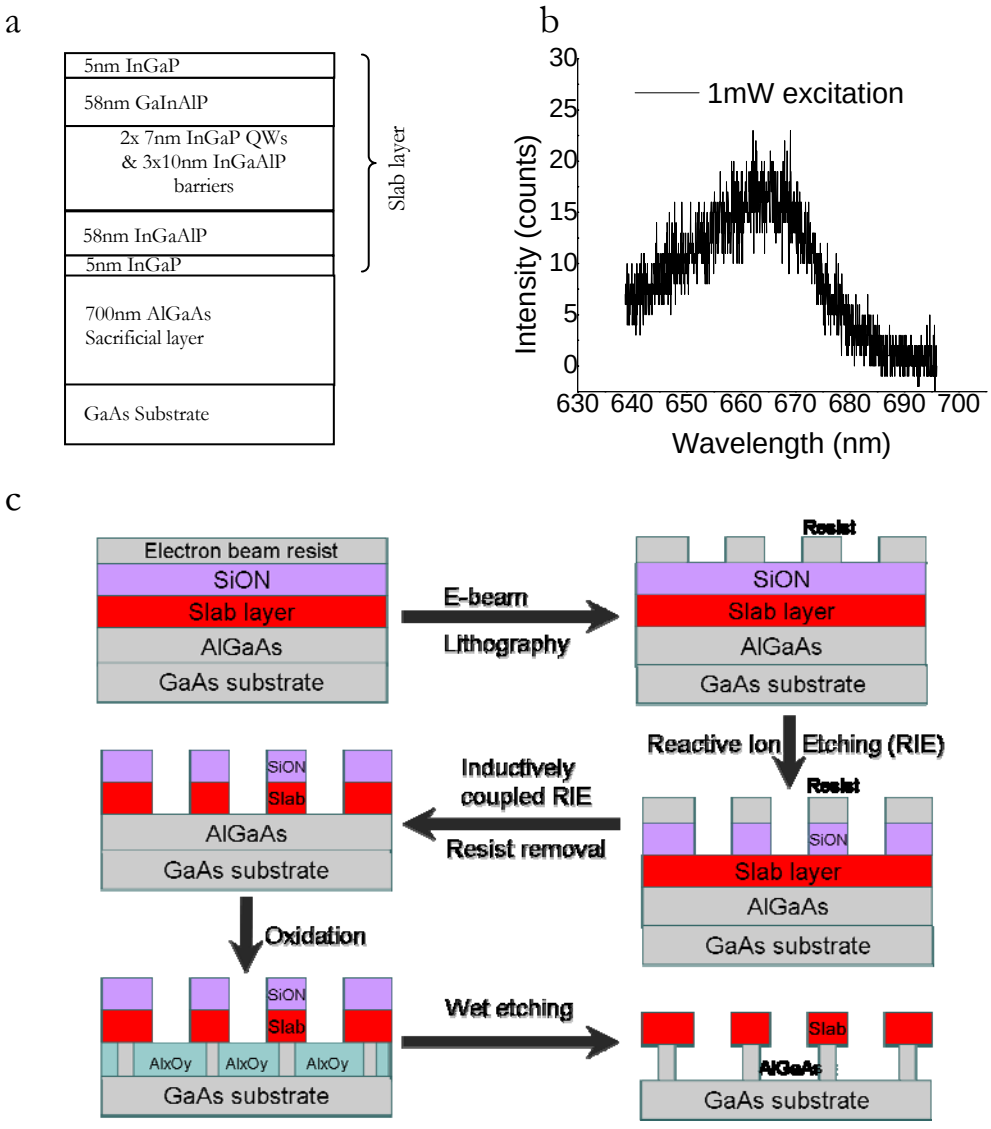

Figure 3.1 (a) Schematic epitaxial layer sequence of our slab composition and (b) a typical photoluminescence emission spectrum taken from the grown wafer. (c) The fabrication procedure flow chart

SiON hard mask and 200 nm ZEP520 electron beam resist.

Electron beam lithography was then used to define ring patterns within the ZEP520 electron beam resist (Figure 3.1c). The inner circles defined the disk diameters and the widths of the rings were designed to prevent optical coupling losses from the disk edge

into the surrounding quantum well material. Reactive ion etching (RIE) was subsequently used to directionally transfer the lithographic pattern from that resist into the SiON etch mask by using a CHF_3 plasma. After removal of the resist, the hard mask pattern was further transferred through the InGaP active layer with an iodine-based inductively coupled plasma reactive ion etch (ICP-RIE). Time-controlled steam oxidation of the AlGaAs by water vapor within a tube furnace followed by the potassium hydroxide (KOH) chemical dissolution of the resulting aluminum oxide formed the mushroom shaped microdisk structure shown in Figure 3.2. Dilute buffered HF was finally used to remove the SiON etch mask. As an alternative to electron beam lithography, it should also be possible to define the microdisk laser disks by photolithography, which provides the opportunity of high throughput production of ultra-small lasers. By defining a post radius to 0.2 μm smaller than that of the microdisk, we minimize the light leakage through the post while maintaining acceptable heat sinking of the active laser mode volume. We have fabricated and characterized many different sizes of disks, with diameters ranging from 1.6 μm down to 0.5 μm, by deliberately decreasing the diameter in 100 nm steps. In these laser arrays, we observe lasing in all of the disks except for the 0.5 μm diameter devices.

The microdisks were optically pumped at room temperature using 8 ns pulses separated by 30 μs periods (0.027% duty cycle) with a 408 nm InGaN semiconductor diode laser. The pump beam was focused onto the sample surface, vertically coupling the excitation light (Figure 3.2b) through a 50x objective lens to form a pump beam spot size less than 3 μm in diameter. Free space pumping does not require fine alignment of the optical fiber

to the disk, an advantage especially for the submicron disk sizes described here. Moreover, free space pumping covers the entire disk area and renders the cavity and the central part of the laser disk transparent to minimize re-absorption in the central disk portion. However, the pumping and collection of laser emission from the disk is not very efficient. The excitation powers used in this chapter were determined by dividing the reading of the power meter at the sample (averaged laser pulse power) by the duty cycle. The emission from the lasers was then collected through the same objective lens and lasing spectra were taken with a liquid-nitrogen-cooled charge coupled device (CCD) (Princeton instruments, Spec10) detector filtered by a monochromator (Acton, SpectraPro). The monochromator entrance slit width was set to a width of 10 μm and a 1200 g/mm grating was used, resulting in a spectral resolution of approximately 0.1 nm. An additional flip-up mirror was used to guide the light into a CCD imaging system to view images of laser cavity modes within the microdisks as well as the excitation pump spot.

Figure 3.2a shows an angled view of a completely fabricated ultra-small microdisk, taken in a scanning electron microscope (SEM). The sidewall roughness of the disk is less than 20 nm and the non-vertical sidewall is due to the non-optimized dry etching recipe which could be further improved. Figure 3.2b illustrates the excitation and detection scheme used in this experiment, and it should be noted that this free space pump-collection measurement scheme is not efficient, since a large portion of the

a

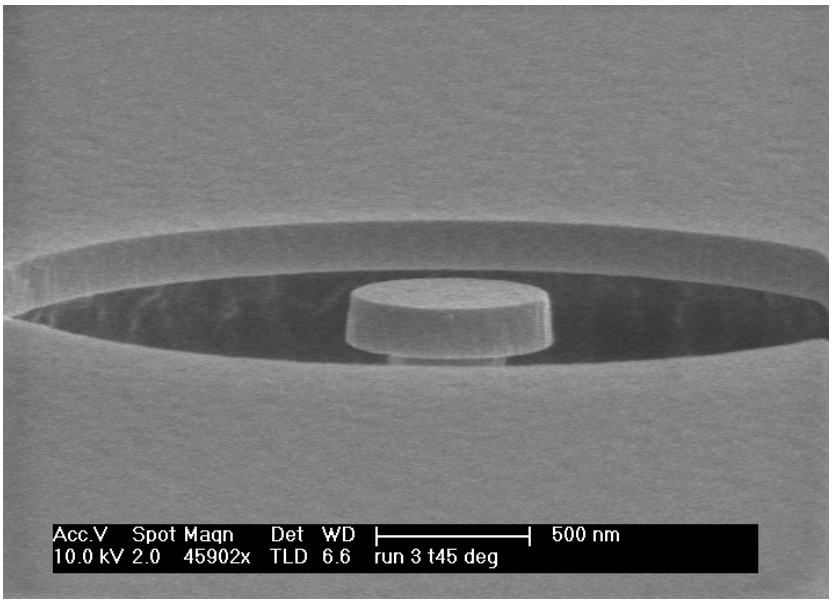

b

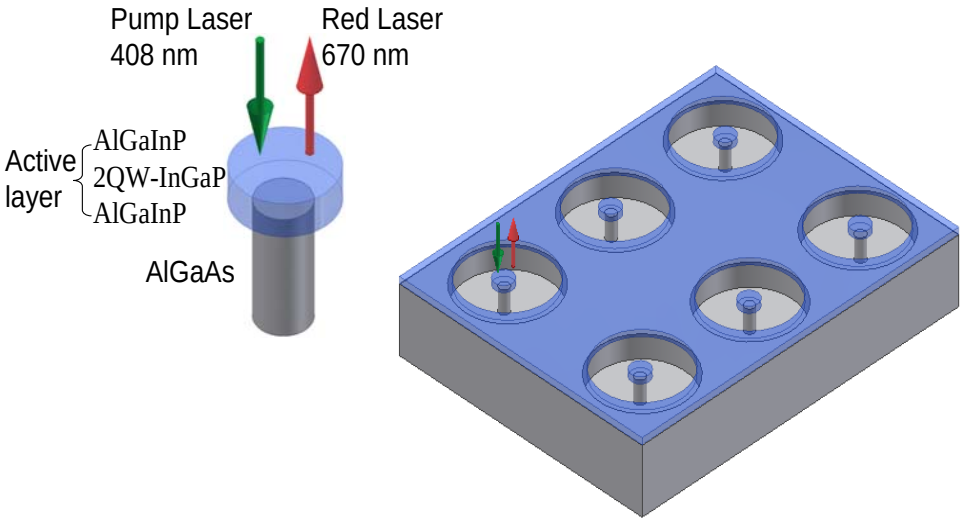

Figure 3.2. (a) Scanning electron microscope image of a 0.6 μm diameter submicron microdisk laser structure. (b) Illustration of mushroom shape structure and pumping scheme

excitation light does not couple into the mode. Indeed, much of the emitted light also escapes horizontally along the disk plane and vertically into the GaAs substrate. We

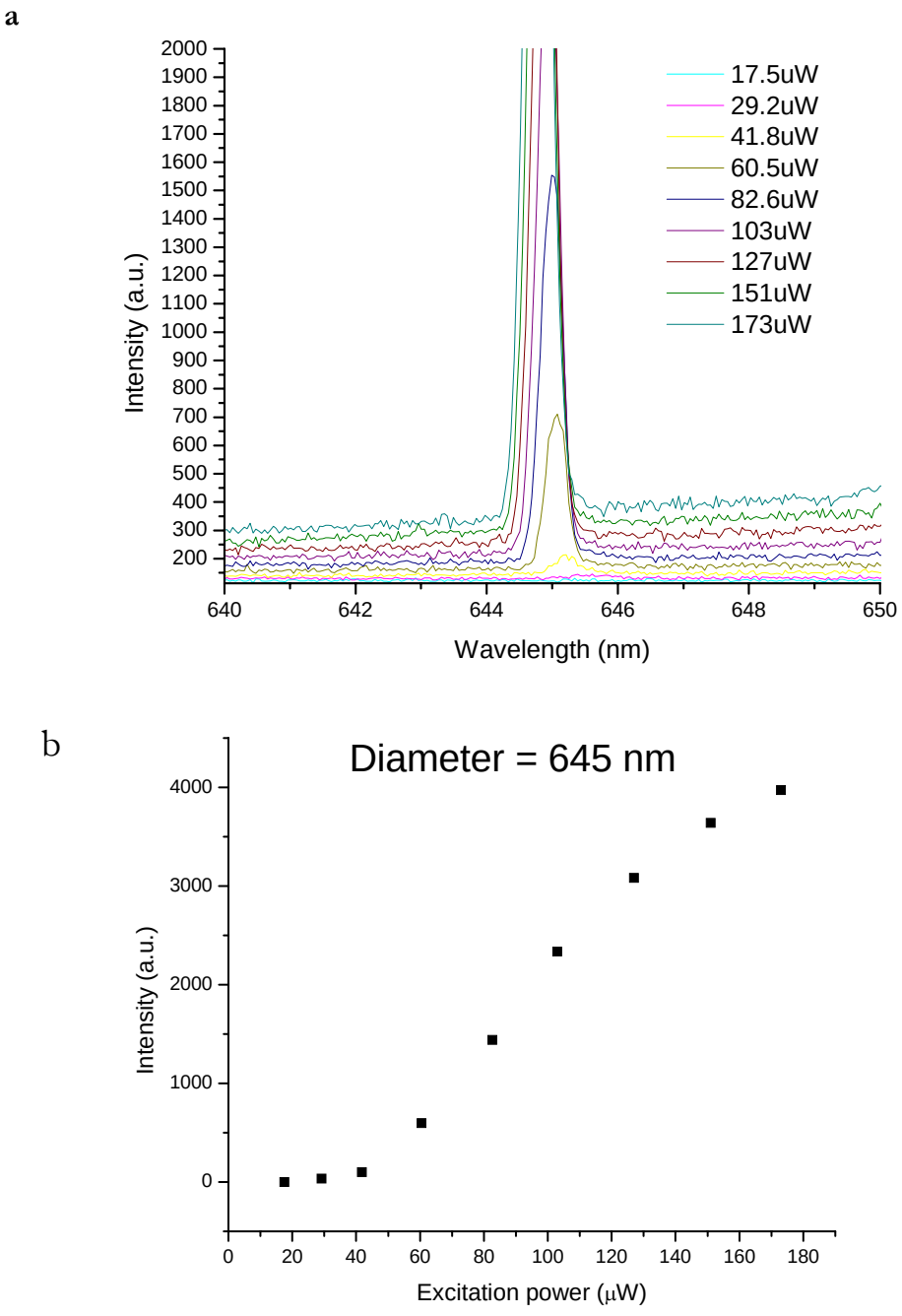

Figure 3.3. (a) The Spectra with different excitation power and (b) L-L curve of one of the 645 nm diameter microdisks

expect that much higher output power and lower thresholds can be observed when using fiber-coupling measurements. Figure 3.3 shows luminescence spectra and an L

(excitation power)-L (lasing peak intensity) curve from a device with disk diameter of 645 nm and post diameter of 200 nm. The laser threshold was measured to be approximately 50 μW. This threshold power is similar to that of photonic crystal slab lasers that we recently fabricated within the same InGaP material system [11]. The linewidth was measured as 0.4 nm at threshold, yielding an effective Q of about 1600. Above 120 μW, heating of the laser cavity ultimately limits the output power, and the L-L curve saturates. Figure 3.4 shows the lasing characteristics of another ultra-small microdisk with disk diameter of 650 nm and post diameter of 350 nm. The laser threshold was measured to be approximately 187 μW and saturation occurred when the power exceeded 250 μW. Linewidth of 0.5 nm was measured at threshold, corresponding to an effective Q of approximately 1300. Both cavities exhibited distinct threshold behavior with linear L-L response of the output power above threshold and before saturation. Figure 3.4 also shows the semi-logarithmic plot of the L-L curve, confirming the lasing characteristics. The difference in threshold and saturation powers in the two smallest lasers may be due to the larger size post of the 650 nm disk. In both cases, we observed a blue shift of the emission as the excitation power increased. This is due to an increase of effective refractive index, which is approximately proportional to the increase in carrier density. The modes for these ultra-small disk lasers need to be further studied [12]. Figure 3.5a shows spectra of some other lasers. Single-mode operation was maintained until the disk diameter was increased to 1 μm. The small peak to the right of the main peak from 1 μm disk may be a result of propagation direction degeneracy, caused by nonsymmetrical or random roughness from the fabrication process.

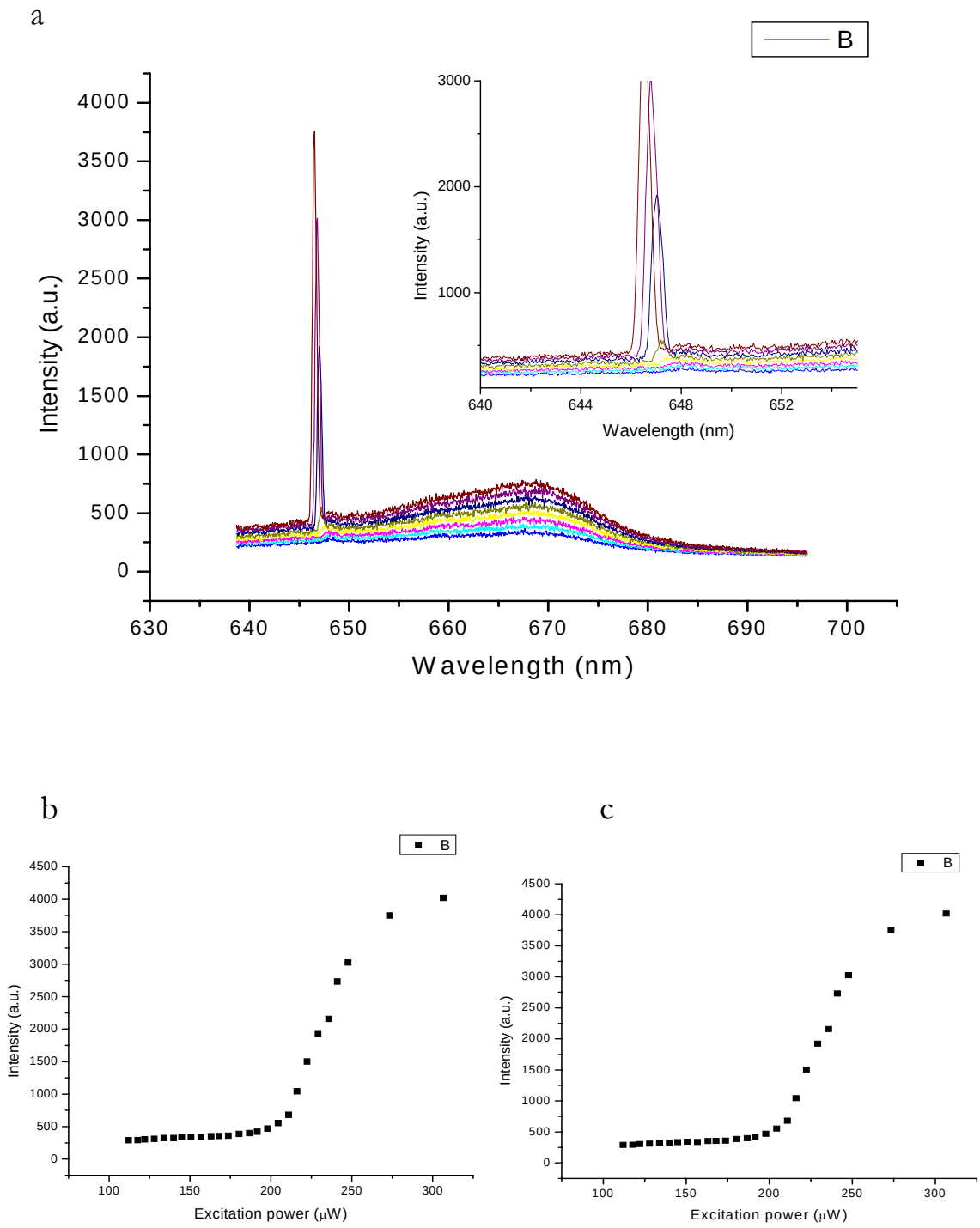

Figure 3.4. (a) The Spectra with different excitation powers and (b)(c) linear and semi-logarithmic plot of L-L curve of a 650 nm diameter microdisk

a

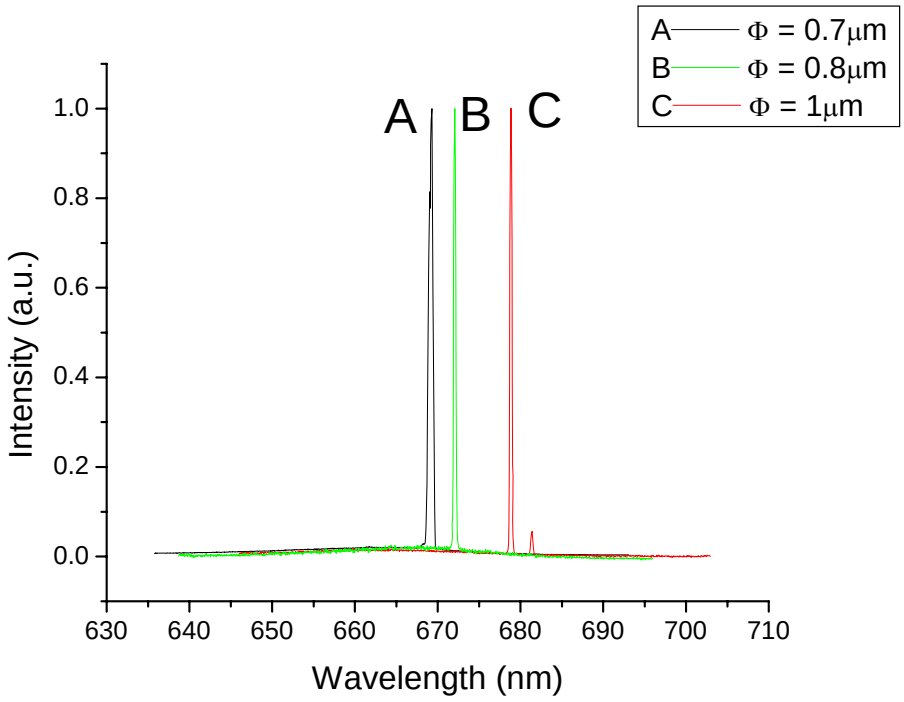

b

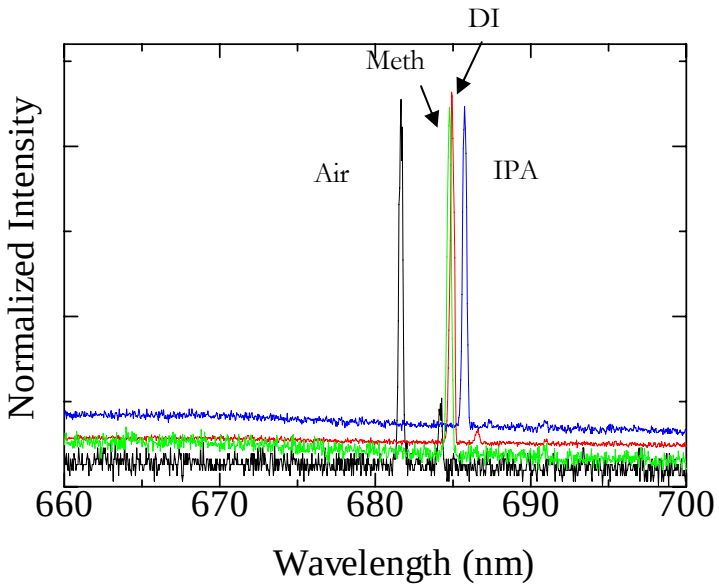

Figure 3.5. (a) Laser spectra with different diameter microdisks and (b) lasing peak wavelength shift obtained with different chemical environments. Black line denotes spectrum in air, green denotes spectrum in methanol, red denotes spectrum in DI water, and blue denotes the spectrum in IPA.

3.3 Microdisk lasers for refractive index monitoring

The use of microdisk lasers for spectroscopic analysis has been described earlier [13]. Here we use the ultra-small mode volume microdisk lasers to check the sensitivity to the environmental refractive index changes and molecules attached onto the disk surface. Figure 3.5b shows the spectra of a 1 μm diameter disk when used as a refractive index monitor. The lasing peak shifts from 681.6 nm to 684.8 nm when the disk is surrounded by methanol, to 684.9 nm in deionized water, and to 685.8 nm when immersed in isopropyl alcohol (IPA). The sensitivity of the microdisk is ~ 11 nm per refractive index unit (REU). We expect higher sensitivities in even smaller disks since the optical mode is more extended to the outside of the disk, and mode hopping can be avoided by utilizing disks that support only few modes. Compared to the results of optimized photonic crystal slab lasers, which provide a sensitivity of 179 nm per REU [14], the sensitivity of our disk laser is one magnitude lower, due to the difference in wavelength as well as the less optimal overlap between the lasing mode and the analyte to be measured. The ease of fabrication, along with the improved tolerance to dimensional imprecision and analyte refractive index, provides the disk structure with important advantages for local refractive index monitoring for chemical and biological analyses.

3.4 Conclusion

In this chapter, we have fabricated ultra-small disk lasers with optical mode volumes of only 0.03 μm^3 in InGaP QW material. We have demonstrated excitation thresholds as low as 50 μW in 645 nm disks at room temperature. We also show the lasing spectra from submicron microdisks with different diameters and explore the use of these ultra-small disk lasers for refractive index monitoring. We expect these InGaP red sub-micron microdisk

lasers to be very useful for biochemical analysis as well as for efficient light emitters in the near future.

Bibliography

1. Mccall, S.L., et al., *Whispering-Gallery Mode Microdisk Lasers.* Applied Physics Letters, 1992. **60**(3): 289-291.
2. Mohideen, U., et al., *Gaas/Algaas Microdisk Lasers.* Applied Physics Letters, 1994. **64**(15): 1911-1913.
3. Pan, J.S., et al., *0.66 mu m InGaP/InGaAlP single quantum well microdisk lasers.* Japanese Journal of Applied Physics Part 2-Letters, 1998. **37**(6A): L643-L645.
4. Hovinen, M., et al., *Blue-Green Laser-Emission from Znse Quantum-Well Microresonators.* Applied Physics Letters, 1993. **63**(23): 3128-3130.
5. Chang, S.S., et al., *Stimulated emission and lasing in whispering-gallery modes of GaN microdisk cavities.* Applied Physics Letters, 1999. **75**(2): 166-168.
6. Michler, P., et al., *A quantum dot single-photon turnstile device.* Science, 2000. **290**(5500): 2282-.
7. Levi, A.F.J., et al., *Room-Temperature Operation of Microdisk Lasers with Submilliamp Threshold Current.* Electronics Letters, 1992. **28**(11): 1010-1012.
8. Baba, T., et al., *Lasing characteristics of GaInAsP-InP strained quantum-well microdisk injection lasers with diameter of 2-10 mu m.* IEEE Photonics Technology Letters, 1997. **9**(7): 878-880.
9. Zhang, L.D. and E. Hu, *Lasing emission of InGaAs quantum dot microdisk diodes.* IEEE Photonics Technology Letters, 2004. **16**(1): 6-8.
10. Levi, A.F.J., et al., *Room-Temperature Operation of Submicrometer Radius Disk Laser.* Electronics Letters, 1993. **29**(18): 1666-1668.

11. Zhang, Z., et al., *Visible two-dimensional photonic crystal slab laser.* Applied Physics Letters, 2006. **89**(7).

12. Gmachl, C., et al., *High-power directional emission from microlasers with chaotic resonators.* Science, 1998. **280**(5369): 1556-1564.

13. Fang, W., et al., *Detection of chemical species using ultraviolet microdisk lasers.* Applied Physics Letters, 2004. **85**(17): 3666-3668.

14. Loncar, M., A. Scherer, and Y.M. Qiu, *Photonic crystal laser sources for chemical detection.* Applied Physics Letters, 2003. **82**(26): 4648-4650.

Chapter 4

VISIBLE TWO-DIMENSIONAL PHOTONIC CRYSTAL SLAB LASERS

4.1 Introduction

Photonic crystal cavities offer many advantages over more conventional cavities for achieving ultra-small modal volumes while maintaining high quality factors [1-5]. When combining such cavities with light emitting active materials, such as quantum wells (QWs) [1] and quantum dots (QDs) [3], it is possible to form ultra-small lasers that can be integrated in dense arrays, and in which each laser cavity supports only very few optical modes. This results in the potential for high frequency modulation of such lasers [6], which has made these devices particularly interesting for applications in optical data communication. Therefore, most research on photonic crystal lasers has thus far focused on near-infrared wavelength emission using InGaAsP or InGaAs active materials. Although some research groups have started to explore the visible wavelength range [7-10], it has been difficult to obtain small mode volume lasers in visible light emitting material systems due to high surface carrier recombination velocities or the lack of high refractive index contrast substrates for light confinement in the vertical direction. Visible photonic crystal lasers operating in the spectral vicinity of 670 nm could enable a broad range of important applications, including high-density optical recording, high resolution visible laser projection displays, and, most importantly, compact spectroscopic sources as ultra-small sensors for biological and chemical detection within small sample volumes. The same devices, when operated in reverse bias, can also function as multispectral detector arrays,

which can be used for polarization-sensitive detection in the visible and near-IR wavelength range. In this chapter, we present our preliminary experimental results of such a two-dimensional photonic crystal slab laser that can satisfy these needs.

4.2 Two-dimensional photonic crystal slab structure

Photonic crystal slab structures were first grown by metallorganic chemical vapor deposition (MOCVD) of InGaP/InGaAlP quantum well material on top of sacrificial AlGaAs layers supported by GaAs substrates. Optical gain was provided by two 7 nm thick and compressively strained InGaP quantum wells which were separated by 10 nm InGaAlP

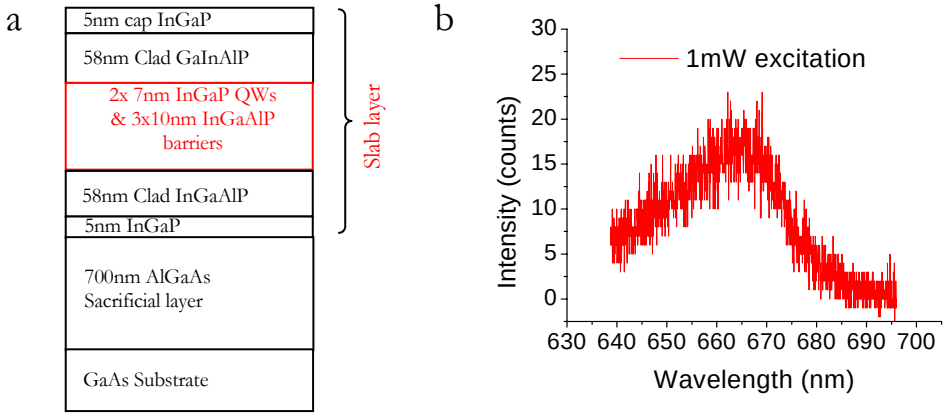

Figure 4.1. Scanning electron microscope image of photonic crystal laser cavity: (a) low-magnification image showing the entire device and (b) higher-resolution image showing the details of the cavity

barriers (Figure 4.1a). The quantum well active material was placed in the center of a 170 nm thick InGaAlP slab, with a 700 nm thick sacrificial AlGaAs layer between the slab and the GaAs substrate. The active quaternary material was designed to emit light at around 670 nm (Figure 4.1b). From the compressive strained quantum wells, light was strongly

coupled into transverse electric (TE) modes. This epitaxially grown material was coated with a 100 nm SiON hard mask and 200 nm of ZEP520 electron beam resist.

Electron beam lithography was then used to define the photonic crystal cavity pattern within the ZEP520 resist. Reactive ion etching (RIE) was subsequently used to transfer the pattern from that resist into the SiON etch mask by using a CHF_3 plasma. After removal of the resist, the hard mask pattern was further transferred through the active layer with an iodine-based inductively coupled plasma reactive ion etch (ICP-RIE). Time-controlled oxidation of the AlGaAs by water vapor followed by the potassium hydroxide (KOH) chemical dissolution of the aluminum oxide formed the suspended slab membranes as shown in Figure 4.2. Finally, diluted buffered hydrofluoric acid was used to remove the SiON etch mask.

The suspended photonic crystal slab cavities were optically pumped at room temperature using 5 ns pulses at 10 kHz (0.005% duty cycle) with a 408 nm InGaN semiconductor diode laser. The pump beam was focused onto the sample surface with a 50x objective lens to form an excitation beam spot size about 2 μm in diameter. The excitation power used in this chapter was determined by dividing the averaged pulse power by the duty cycle. The emission from the lasers was then collected through the same lens and their spectra detected with a liquid-nitrogen-cooled charge-coupled device (CCD) (Princeton instruments, Spec10) detector filtered by a monochromator (Acton, SpectraPro). The monochromator entrance slit width was set to 10μm and the 1200 g/mm grating was used, resulting in a spectral resolution of approximately 0.1 nm. An additional flip-up

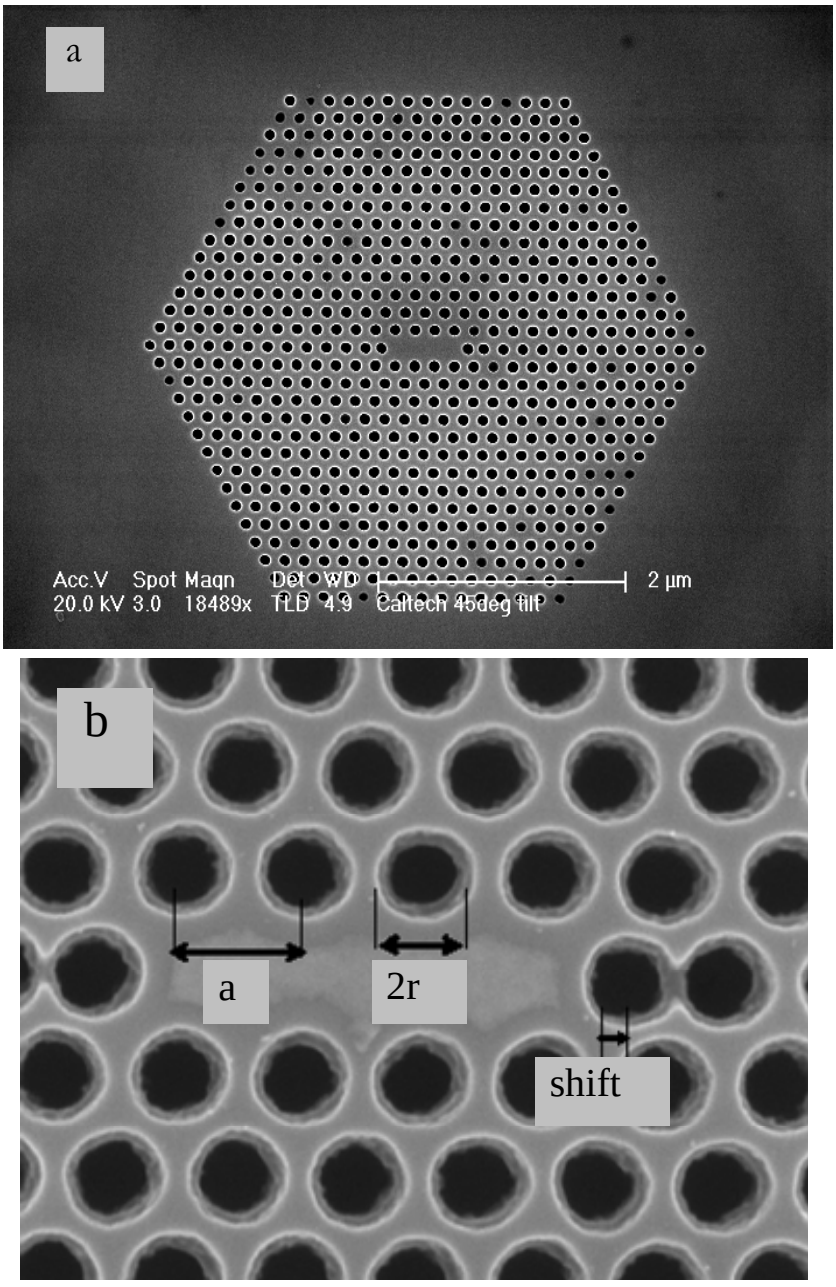

Figure 4.2. Scanning electron microscope image of photonic crystal laser cavity (a) low magnification image showing the entire device and (b) higher resolution image showing the details of the cavity.

mirror was used to guide the light into a CCD imaging system to view the near-field images of the lasers as well as the excitation laser spot. The imaging optics also permitted the observation of laser cavity modes.

4.3 Characterization of the 2D photonic crystal slab laser

For this work, we used a high Q cavity design proposed by Noda's group [5] consisting of a L3 linear defect (removing 3 holes) within a triangular photonic crystal lattice of holes on a thin high-index slab. This design reduces the loss in the vertical direction by shifting the holes at the end of the defect area outwards. Figure 4.2 shows the top view of a fabricated photonic crystal microcavitiy slab. The lattice spacing, a, the radius of hole, r, and the shift of the hole were defined as shown in the Figure 4.2b. We lithographically controlled the ratio between the hole shift and the lattice spacing (shift/a) to be 0.2. Also, we lithographically varied the lattice spacing (a) within a range from 0.14 μm to 0.18 μm and the ratio between the hole radius and lattice spacing (r/a, the porosity factor) from 0.25 to 0.29. Fourteen periods of photonic crystal lattice (Figure 4.2a) were used to surround the defect within the 170 nm thick quantum well active layer slab, which has a refractive index of around 3.4 at 670 nm. The photonic crystal and cavity dimensions were designed to match the 670 nm emission wavelength of the InGaP active material. Figure 4.3 shows luminescence spectra and the L(excitation power)-L(lasing peak intensity) curve from a device with lattice parameter a=170 nm and porosity factor r/a=0.26. The laser threshold was determined to be approximately 250 μW, and the linewidth was measured as 0.3 nm at threshold, yielding an effective Q of about 2000. Below threshold, only a broad background from the gain medium was measured from this cavity. Above 450 μW, heating of the laser cavity limited the output power, and the L-L curve saturated. The 2D photonic crystal cavity peak can be tuned by changing either the porosity or the lattice parameter of the photonic crystal lattice surrounding the nanocavity. Figure 4.4 shows a laser with a slightly lower porosity (porosity factor r/a=0.25). For this laser, the measured

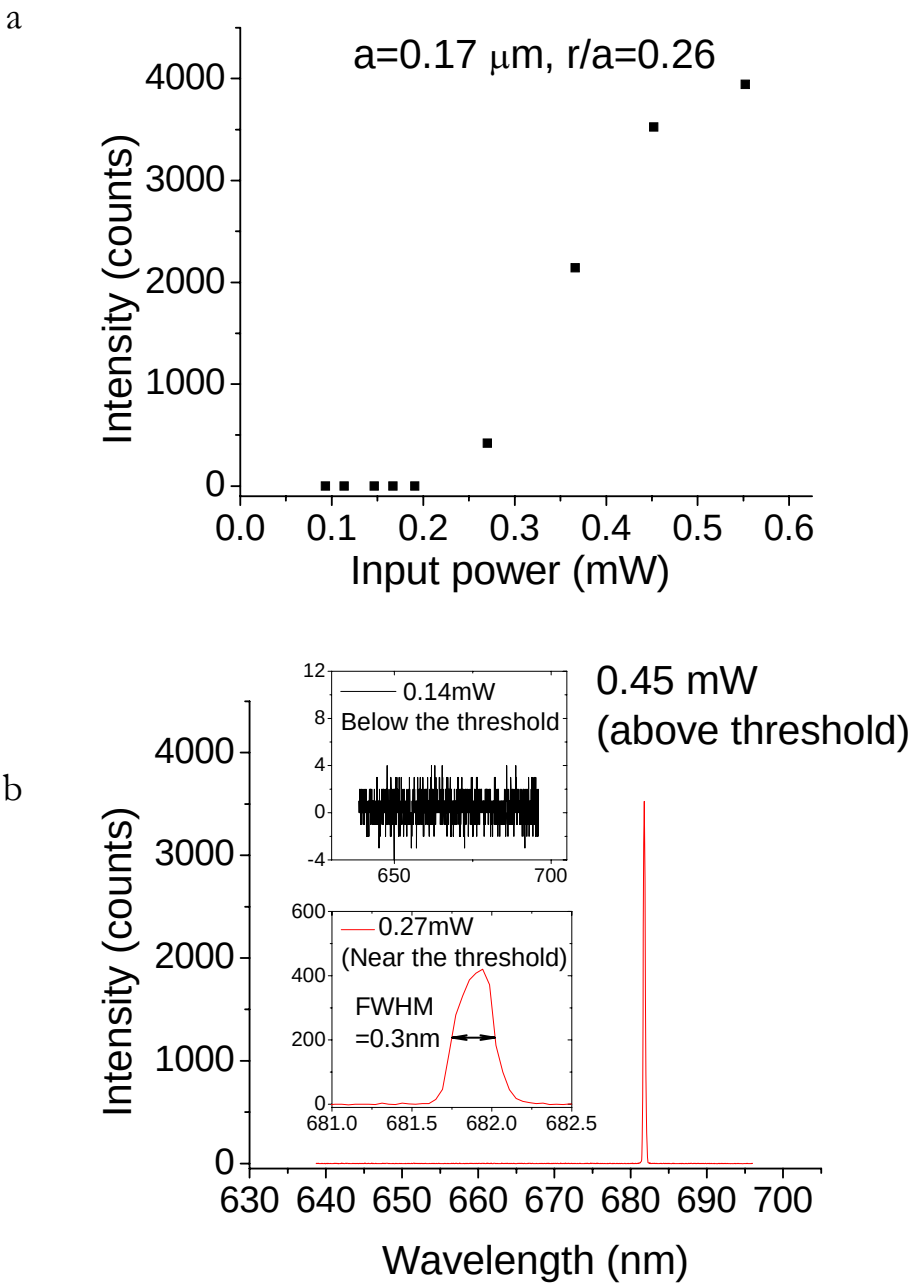

Figure 4.3. (a) L-L curve. (b) Typical lasing spectrum of an InGaP 2D photonic crystal laser with a lattice parameter of a=0.17 μm and porosity factor r/a=0.26

laser threshold was 400 μW, and the device again saturated as a result of cavity heating above 1 mW. Both cavities exhibited distinct threshold and linearity in the output power

a

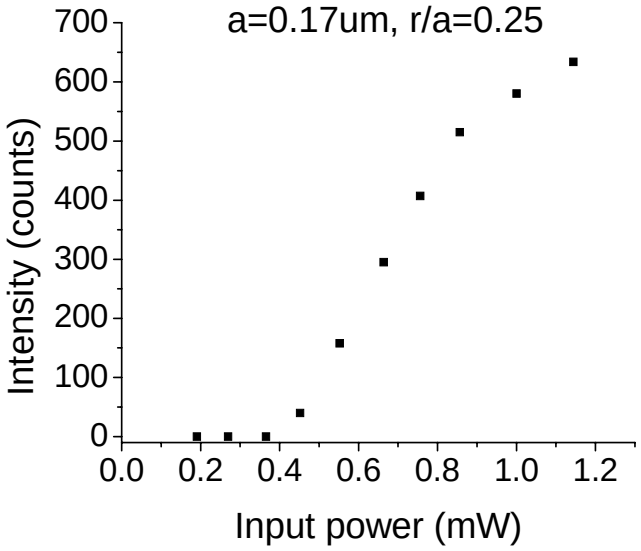

b

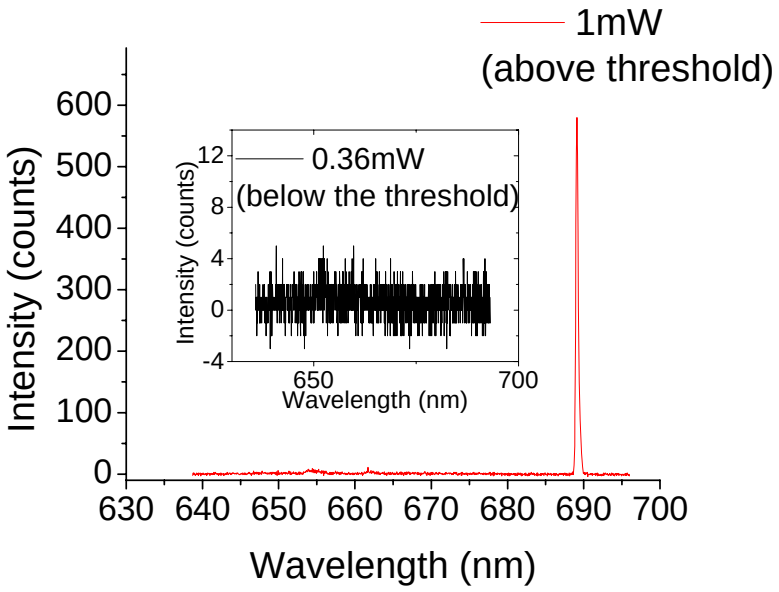

Figure 4.4. (a) L-L curve. (b)Typical lasing spectrum for an InGaP 2D photonic crystal laser with a lattrice parameter of a=0.17 μm and a porosity factor r/a=0.25

above threshold but before saturation. The lasing characteristic was very sensitive to the position of the excitation beam spot (~1 μm movement), which indicates that lasing occurs from a localized defect mode. Many of the photonic crystal cavity geometries that we defined did not result in demonstration of lasing, and we show a typical spectrum result

from a non-lasing cavity in Figure 4.5, along with the L-L curve. In this case, no inflection was measured and a more or less linear increase of emission with increasing excitation power was observed, saturating again at high excitation powers due to heating of the cavity. No lasing peak was observed, and the Fabry-Perot filtered luminescence emission was not bright enough to observe with our experimental spectroscopic measurement setup.

4.4 Tuning of the emission peak wavelength

Figure 4.6a shows the influence of changing of the porosity on the laser emission wavelength, whereas Figure 4.6b shows a similar tuning curve for changes in the photonic crystal lattice parameter. The uneven spectral shifts result from fabrication variation and device scaling only in two rather than three dimensions due to the fixed slab thickness. This data indicates that the InGaP photonic crystal lasers can be lithographically tuned throughout the gain emission of the quantum wells. The accuracy of such tuning is only limited by the quality and reproducibility of the fabrication process. It should be noted that the minimum feature size required for the successful definition of the photonic crystal mirror surrounding the laser cavities is approximately 30 nm, which is the distance between two adjacent holes in the slab. Compared to conventional InGaAsP material systems operating at 1550 nm, our fabrication process has to overcome the feature size scaling associated with the 2.3 times decreases in wavelength. Nevertheless, with our fabrication approach, it is possible to define dense arrays of laser cavities that are separated by as little as 2 microns. Compact multi-spectral sources can therefore be defined within the visible wavelength range.

a

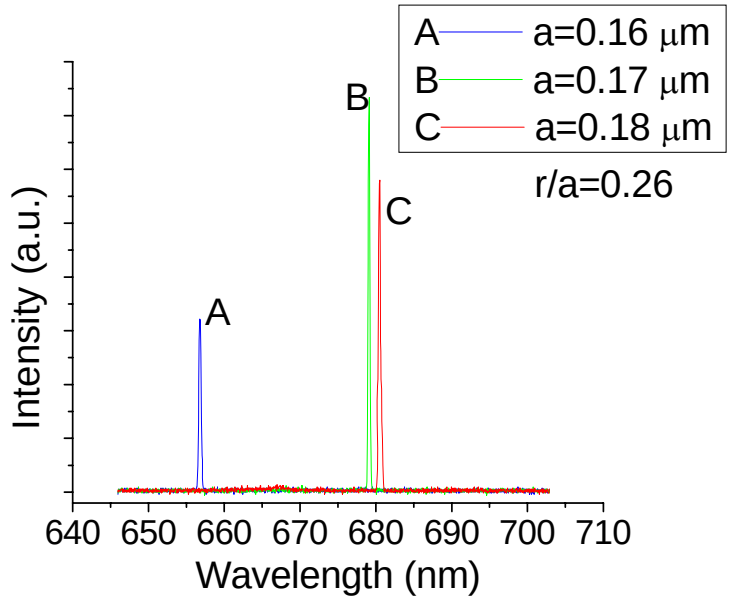

b

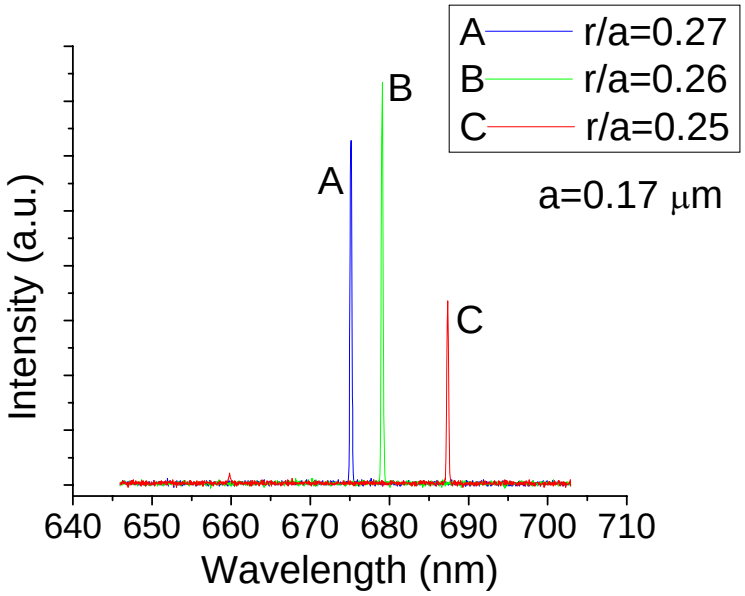

Figure 4.5. (a) r/a fixed to 0.26. (b) Lattice spacing fixed to 0.17 μm (the uneven spectral shifts result from fabrication variation and device scaling only in two dimensions due to the fixed slab thickness)

4.5 Conclusion

The use of photonic crystal lasers for spectroscopic analysis has been described earlier [11], and offers the opportunity to define ultra-small optical cavities with enormous optical field intensities. These devices have been used in the past as refractive index sensors, indicating the refractive index of volumes as small as 10^{-17} liters, limited by the mode volume of 0.03 cubic microns at 1550 nm wavelength. In our experiments, we have defined lasers within a wavelength range that is even more interesting for spectroscopic applications, as many of the fluorophores used for biological analysis are limited to the visible spectrum, and single-photon detectors are available at such wavelengths. Moreover, these devices may become very interesting sources for Raman spectroscopy and other specific measurements of the chemical composition of the femtoliter contents of an optical nanocavity. We expect InGaP lasers to be very useful for biochemical analysis as well as for efficient displays and high-frequency lasers in the near future.

Bibliography

1. Painter, O., et al., *Two-dimensional photonic band-gap defect mode laser.* Science, 1999. **284**(5421): 1819-1821.
2. Loncar, M., et al., *Low-threshold photonic crystal laser.* Applied Physics Letters, 2002. **81**(15): 2680-2682.
3. Yoshie, T., et al., *Quantum dot photonic crystal lasers.* Electronics Letters, 2002. **38**(17): 967-968.
4. Vahala, K.J., *Optical microcavities.* Nature, 2003. **424**(6950): 839-846.
5. Akahane, Y., et al., *High-Q photonic nanocavity in a two-dimensional photonic crystal.* Nature, 2003. **425**(6961): 944-947.

6. Yoshie, T., et al., *High frequency oscillation in photonic crystal nanolasers.* Applied Physics Letters, 2004. **84**(18): 3543-3545.

7. Campbell, M., et al., *Fabrication of photonic crystals for the visible spectrum by holographic lithography.* Nature, 2000. **404**(6773): 53-56.

8. Wu, X., et al., *Ultraviolet photonic crystal laser.* Applied Physics Letters, 2004. **85**(17): 3657-3659.

9. Choi, Y.S., et al., *GaN blue photonic crystal membrane nanocavities.* Applied Physics Letters, 2005. **87**(24)

10. Meier, C., et al., *Visible resonant modes in GaN-based photonic crystal membrane cavities.* Applied Physics Letters, 2006. **88**(3)

11. Loncar, M., A. Scherer, and Y.M. Qiu, *Photonic crystal laser sources for chemical detection.* Applied Physics Letters, 2003. **82**(26): 4648-4650

Chapter 5

SINGLE-MODE OPTOFLUIDIC DISTRIBUTED FEEDBACK DYE LASER

5.1 Introduction

Recently, several groups have demonstrated on-chip liquid dye lasers using different materials and laser cavity geometries [1-3]. Such lasers allow the integration of coherent light sources with other microfluidic and optical functionalities, and are of great interest for making fully functional “lab-on-a-chip” systems. However, the lack of both transverse mode and longitudinal mode selection in the previous demonstrations led to multiple mode operation and wide emission linewidths (~ 5 nm) that are hard to distinguish from amplified spontaneous emission (ASE). Balslev and Kristensen [4] recently demonstrated a microfluidic dye laser using a ~ 130th order Bragg grating imprinted on a glass substrate without transverse confinement. Approximately single spatial mode operation was observed due to the high losses of higher-order spatial modes. In this chapter we present, to our knowledge, the first chip-based single-mode liquid dye laser using a distributed feedback (DFB) structure. DFB cavities combined with 3D optical waveguides are very efficient structures for making single frequency microfabricated lasers [5]. Their implementation on a microfluidic chip will greatly improve the performance of microfabricated liquid dye lasers.

5.2 Chip design and fabrication of single mode DFB dye laser

The schematic diagram of our device is shown in Figure 5.1. The laser chip is entirely made of poly(dimethylsiloxane) (PDMS), a silicone elastomer which has become

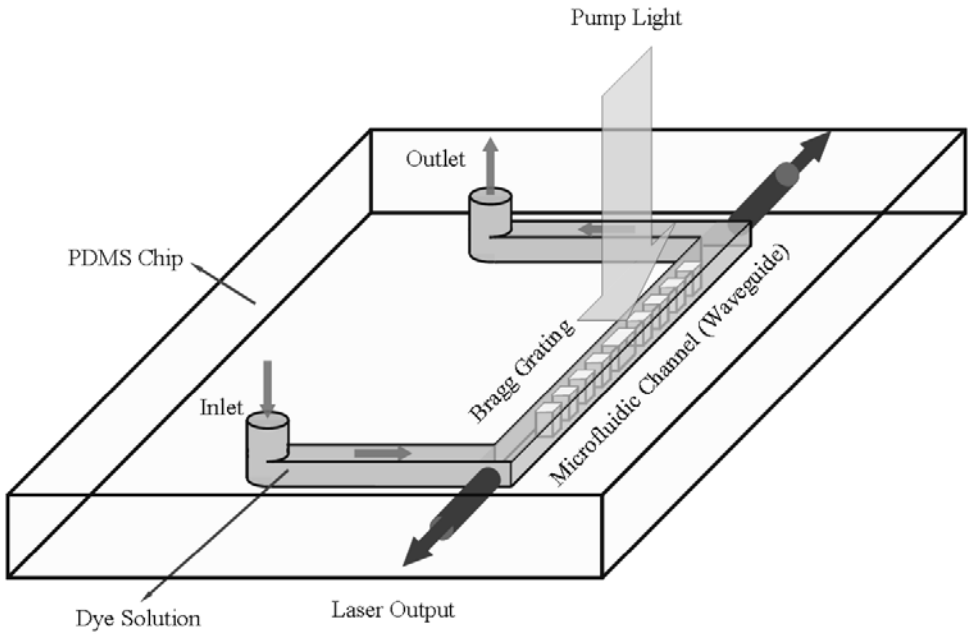

Figure 5.1. Schematic diagram of a monolithic optofluidic DFB dye laser

popular for microfluidics and nanofabrication [6, 7], and has good optical properties in the visible region. A sufficiently small microfluidic channel, when filled with a dye solution of higher refractive index than that of PDMS (n_{PDMS} = 1.406), acts as a single-mode optical waveguide. The gain medium is a 1 mM solution of Rhodamine 6G in a methanol and ethylene glycol mixture with refractive index of 1.409. The periodic PDMS posts inside the channel form a 4 mm long 15th order Bragg grating which provides the optical feedback necessary for the laser action. In addition, a 15π phase shift is introduced at the center of the grating to ensure single frequency operation. The PDMS posts also provide support for the microfluidic channel.

The fabrication of the optofluidic DFB dye laser uses the same replica molding soft

lithography technique which is widely used to make microfluidic devices [8, 9]. Briefly, a master mold was fabricated using conventional photolithography. 2 μm thick

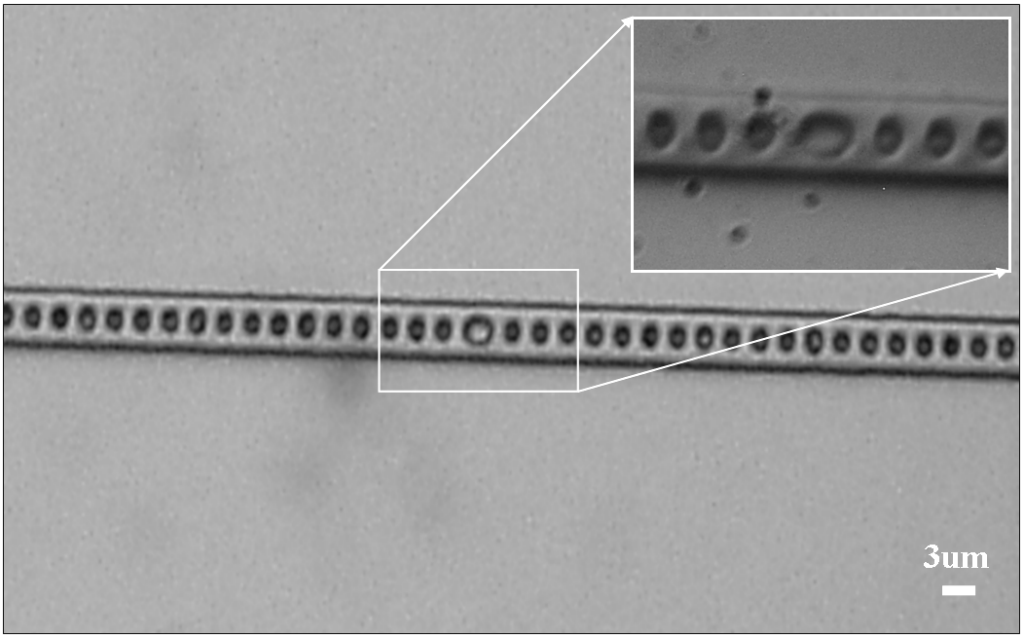

Figure 5.2. Optical micrograph of a microfluidic channel with a 15th order DFB structure on a PDMS chip. The grating period is 3 μm. The central larger PDMS post introduces a 15π phase shift. The inset shows the picture of a real optofluidic dye laser chip.

SU8-2002 negative photoresist (MicroChem) was spin-coated on a silicon wafer and patterned with a Cr-on-glass mask. The mold was treated with tetramethylchlorosilane (Aldrich) for 3 minute before use to facilitate the release of PDMS. Then 5:1 part A:B PDMS prepolymer (GE RTV 615) was poured onto the mold and baked at 80^{o}C for 30 minute. The partially cured PDMS was peeled from the master and the liquid inlet and outlet ports were punched through the whole layer using a 23-gauge luer-stub adapter. This patterned PDMS, containing the laser structure, was then treated with oxygen plasma and bonded to another featureless PDMS to form a monolithic device. Finally, the resulting device was cut to size and baked at 80^{o}C overnight. Figure 5.2 shows an optical

microscope image of the central phase shift region of the laser cavity.

5.3 Longitudinal and transverse mode selection

To make a single-mode laser, both the transverse mode and longitudinal mode selection need to be carefully designed. The waveguide dimensions (width 5 μm; height 2 μm) are chosen such that when filled with liquid of refractive index 1.409 it only supports the two fundamental E_{11} modes. If we define the x direction along the width and the y direction along the height, the E_{11}^{x} mode (transverse E field along x direction) is more confined than the E_{11}^{y} mode, and thus is the preferred lasing mode. The small cross-section area also reduces the required pump power to achieve the lasing threshold.

To obtain stable single frequency operation, the free spectral range of the employed cavity structure has to be larger than the gain spectral bandwidth. Organic dye molecules are well known to have very broad gain spectra with a typical bandwidth of 30 nm to 50 nm (full width at half maximum FWHM). This forces the characteristic length of the resonant structure to be shorter than 4 μm. When a DFB structure is used to provide the optical feedback, the lasing wavelength is determined by the Bragg condition:

$$m\lambda_m = 2n_{eff}\Lambda \tag{5.1}$$

where λ_m is the mth order resonant wavelength, n_{eff} is the effective index of the guided mode [5] and Λ is the grating period. The free spectral range (*FSR*) is given by:

$$FSR = \frac{\lambda_m}{m-1}, \quad (or \ \ \Delta\nu = \frac{c}{2n_{eff}\Lambda}). \tag{5.2}$$

Therefore for a DFB structure with Λ = 3 μm (1.5 μm + 1.5 μm) and n_{eff} = 1.407, the 15th

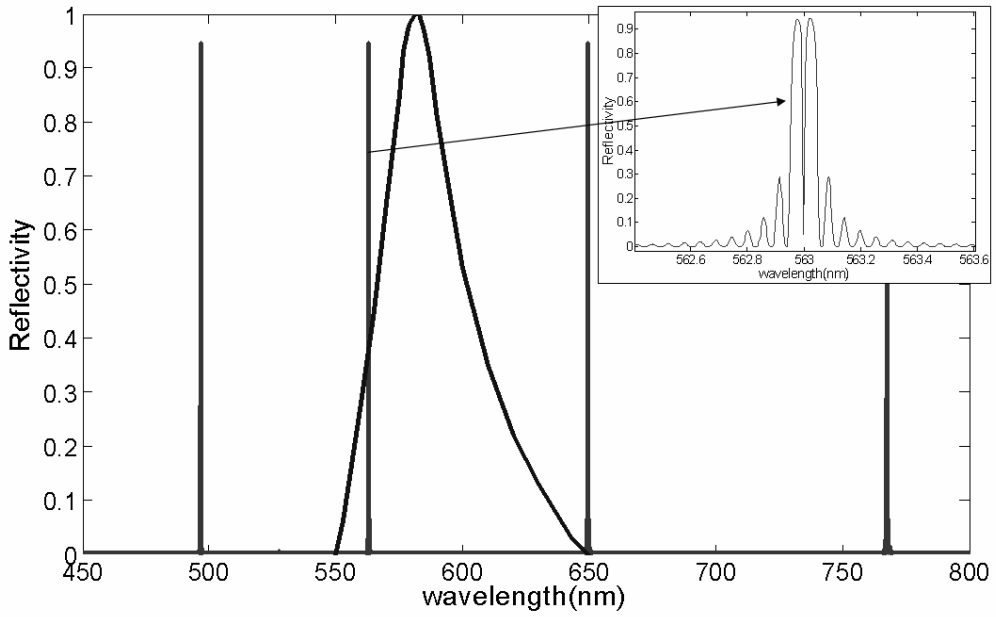

Figure 5.3. Simulated reflectivity spectrum of a 15π phase shifted 15th order DFB structure. The curve spanning from 550 nm to 650 nm is the gain spectrum of Rhodamine 6G. The inset shows the enlarged plot the 15th resonance at 563 nm

resonant wavelength and *FSR* are 563 nm and 40.2 nm respectively. In addition the even order resonances are absent when using a 50% duty-circle square-wave shaped grating. The resulting effective *FSR* of ~ 90 nm ensures a single resonance inside the gain spectrum of Rhodamine 6G which spans from 550 nm to 650 nm. However, within each resonance, there are still side modes, due to the finite length of the grating. It's well known that a DFB laser with a uniform grating operates not at the Bragg wavelength but instead at the two degenerate wavelengths situated symmetrically on either side of the Bragg wavelength [10].

To break this degeneracy, a $14\pi + \pi$ phase shift is introduced at the center of the grating. Figure 5.3 shows the simulated reflectivity spectrum of the overall structure using Rouard's method [11]. The parameters used are: Λ = 1.5 μm + 1.5 μm, grating length L = 4 mm, 15π phase shift at the center, core index n_{core} = 1.409, and cladding/post index n_{clad} = 1.406. It is clearly seen that only the 15th resonance falls in the gain spectrum of Rhodamine 6G. The inset of Figure 5.3 shows the detailed 15th resonance, where the high-pass dip inside the stop band corresponds to the lasing mode.

An interesting property of the higher order DFB structure is that it enables multicolor lasing in the same cavity, each at a single frequency. For example, Figure 5.3 shows that the DFB structure employed in this work can support 497 nm, 563 nm and 650 nm lasing as long as a suitable dye is chosen for each wavelength. This is a highly desired feature for applications where multi-wavelength laser sources are needed, such as multi-color flow cytometry [12] or fluorescence resonance energy transfer (FRET) with multiple donors and acceptors. However, compared with the first order DFB structure, higher order DFB cavities are less efficient in terms of light confinement because the coupling coefficient is inversely proportional to the order of the Bragg scattering [13]. This can be compensated for by increasing the cavity length to provide strong enough feedback.

5.4 Characterization of the dye lasers

The dye solution was introduced into the microfluidic channel by applying 10 psi pressure at the inlet port. We found, to operate the laser in the pulsed mode, it is not necessary to circulate the dye solution. The laser chip was optically pumped with 6 ns Q-switched Nd:YAG laser pulses of 532 nm wavelength, focused to a ~ 100 μm wide stripe aligned

with the microfluidic channel. A 10x microscope objective was used to collect the emission light from one edge of the chip and deliver it to a fiber coupled CCD-array based spectrometer with 0.1nm resolution (Ocean Optics HR4000). A typical single mode lasing spectrum is shown in Figure 5.4 where the lasing wavelength is 567.3nm, very close to the predicted value 563nm. The measured linewidth is 0.21nm. A plot of laser output energy

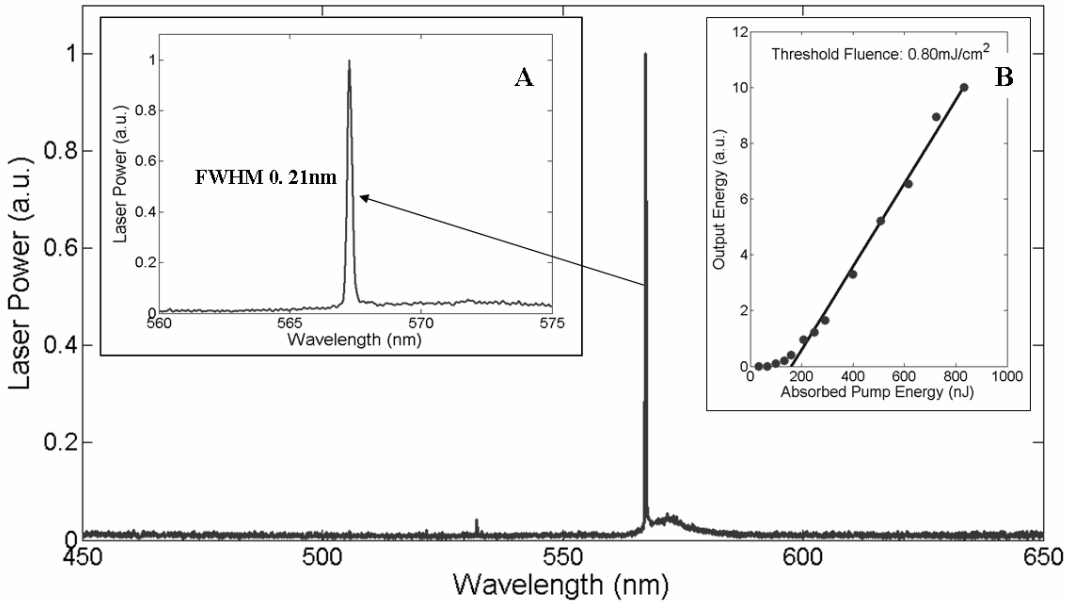

Figure 5.4. Optofluidic DFB dye laser spectrum. The measured linewidth is 0.21 nm. The inset B shows the output energy vs. the absorbed pump energy curve. The threshold pump fluence is ~ 0.8 mJ/cm^2.

versus the absorbed pump energy is shown as the inset B of Figure 5.4. The threshold pump fluence is estimated to be ~ 0.8 mJ/cm^2, which gives peak pump intensity around 150 kW/cm^2. The laser remains single mode at pump levels as high as 8 mJ/cm^2. At moderate pump intensities (200-400 kW/cm^2) and 10 Hz repetition rate, stable laser output lasted longer than 20 minute and the chip can be reused for many times without noticeable degradation.

The elasticity of silicone elastomer and the microfluidics compatibility of the laser chip immediately suggest two wavelength tuning mechanisms. First, the grating period is easily tunable by stretching or compressing the whole chip due to the low Young's modulus of PDMS (~ 750 kPa) [6]. Second, the refractive index of the dye solution can be tuned by mixing two solvents with different refractive indices. For example, using methanol and dimethylsulfoxide (DMSO), the achievable refractive index change can be as large as 0.148 (1.33 for methanol versus 1.478 for DMSO). Furthermore, different dye molecules can be used to cover an even larger spectral range. The mixing, switching and delivery of dye solutions can all be implemented on a silicone elastomer chip using the recently developed mechanical micro valves and pumps [9].

5.5 Conclusion

In this work, we have proposed and demonstrated a phase-shifted 15th order DFB structure as the optical cavity in an optofluidic dye laser system. Single mode operation was obtained with pump fluence from 0.8 mJ/cm^2 to 8 mJ/cm^2. The measured laser linewidth is 0.21 nm. The fabrication and operation of the laser chip is fully compatible with silicone elastomer-based microfluidics technology.

Bibliography

1. Helbo, B., A. Kristensen, and A. Menon, *A micro-cavity fluidic dye laser*. Journal of Micromechanics and Microengineering, 2003. **13**(2): 307-311.
2. Vezenov, D.V., et al., *A low-threshold, high-efficiency microfluidic waveguide laser*. Journal of the American Chemical Society, 2005. **127**(25): 8952-8953.
3. Galas, J.C., et al., *Microfluidic tunable dye laser with integrated mixer and ring resonator*. Applied Physics Letters, 2005. **86**(26).
4. Balslev, S. and A. Kristensen, *Microfluidic single-mode laser using high-order Bragg grating and antiguiding segments*. Optics Express, 2005. **13**(1): 344-351.
5. Coldren, L.A. and S.W. Corzine, *Diode lasers and photonic integrated circuits*. Wiley series in microwave and optical engineering. 1995, New York: John Wiley & Sons. xxiii, 594
6. McDonald, J.C. and G.M. Whitesides, *Poly(dimethylsiloxane) as a material for fabricating microfluidic devices*. Accounts of Chemical Research, 2002. **35**(7): 491-499.
7. Quake, S.R. and A. Scherer, *From micro- to nanofabrication with soft materials*. Science, 2000. **290**(5496): 1536-1540.
8. Xia, Y.N. and G.M. Whitesides, *Soft lithography*. Annual Review of Materials Science, 1998. **28**: 153-184.
9. Unger, M.A., et al., *Monolithic microfabricated valves and pumps by multilayer soft lithography*. Science, 2000. **288**(5463): 113-116.
10. Yariv, A, *Optical electronics in modern communications*. 5th ed. Oxford series in electrical and computer engineering. 1997, New York: Oxford University Press. xviii, 744
11. Wellerbrophy, L.A. and D.G. Hall, *Analysis of wave-guide gratings - application of rouard method*. Journal of the Optical Society of America a-Optics Image Science and Vision, 1985. **2**(6): 863-871.
12. De Rosa, S.C., et al., *11-color, 13-parameter flow cytometry: Identification of human naive T cells by phenotype, function, and T-cell receptor diversity*. Nature Medicine, 2001. **7**(2): 245-248.
13. Streifer, W., D.R. Scifres, and R.D. Burnham, *Coupling coefficients for distributed feedback single-heterostructure and double-heterostructure diode lasers*. IEEE Journal of Quantum Electronics, 1975. **11**(11): 867-873.

Chapter 6

MECHANICALLY TUNABLE OPTOFLUIDIC DISTRIBUTED FEEDBACK DYE LASER

6.1 Introduction

On-chip liquid dye lasers are promising coherent light sources for “lab-on-a-chip” systems in that they allow the integration of laser sources with other microfluidic and optical functionalities. Several groups have demonstrated such dye lasers using different materials and laser cavity designs [1-3]. Tunable output was also obtained using concentration or index tuning methods [3, 4]. Indeed, on-chip liquid dye lasers are examples of the new class of emerging optofluidic devices, in which the integration of microfluidics with the adaptive nature of liquids enables unique performance that is not obtainable within solid state materials [5]. Recently, an optofluidic distributed feedback (DFB) dye laser was demonstrated on a silicone elastomer chip [6]. Stable single-mode operation with narrow linewidth was obtained using a phase-shifted higher order Bragg grating embedded in a single mode microfluidic channel waveguide. In this chapter, by combining the mechanical flexibility of the elastomer materials and the reconfigurability of the liquid gain medium, we demonstrate the tunability of such single mode DFB liquid dye lasers.

6.2 Chip design

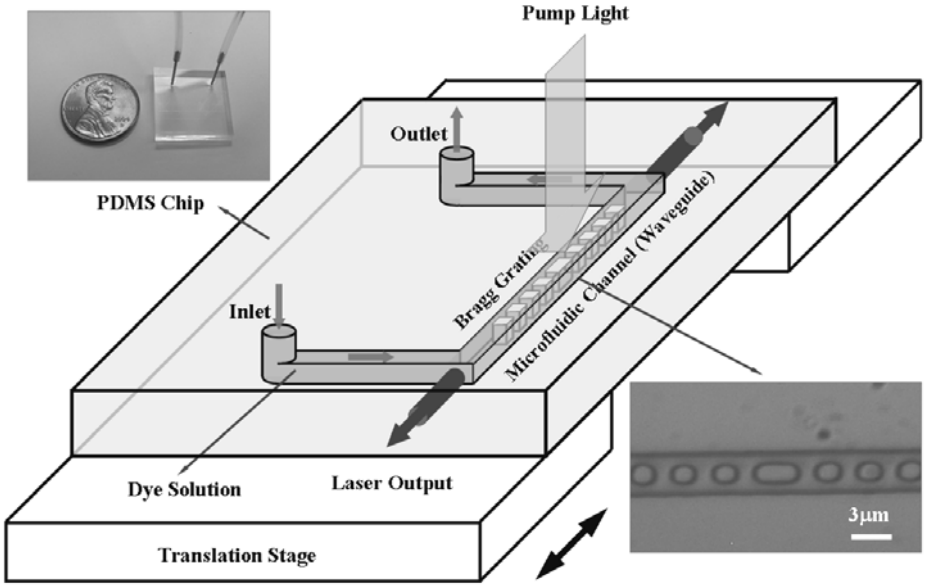

Figure 6.1. Schematic diagram of a mechanically tunable optofluidic DFB dye laser chip. The upper inset shows an actual monolithic PDMS laser chip. The lower inset is an optical micrograph of the central phase-shifted region of the laser cavity. A Bragg grating with 3080 nm period is embedded in a 3 μm wide microfluidic channel. The channel height is 2 μm. The size of the PDMS posts is about 1.28 μm×1.8 μm inferred from the optical micrograph. The central, larger PDMS post introduces an effective $\pi/2$ phase shift to ensure single wavelength lasing. The movement of the translation stage deforms the chip, which causes the grating period to change.

As shown in Figure 6.1, the optofluidic DFB dye laser was fabricated on a monolithic PDMS chip using the replica molding soft lithography technique as described in [6]. A microfluidic channel, when filled with liquid of higher refractive index than that of PDMS (1.406, GE RTV615), acts as a buried channel waveguide. The channel dimensions are 2 μm×3 μm and the index contrast is less than 0.003, so that the waveguide supports only the fundamental TE_{00} and TM_{00} modes. The distributed feedback is provided by the periodic PDMS posts inside the channel with 3080 nm period, which form a 1 cm long 15^{th} order Bragg grating at wavelength around 570 nm. The PDMS posts also provide mechanical support for the microfluidic channel. An effective

$\pi/2$ phase shift is introduced at the center of the grating to ensure single frequency operation at the Bragg wavelength [7]. The gain medium is a 2 mM solution of Rhodamine 6G (Rh6G) or Rhodamine 101 (Rh101) in a methanol and ethylene glycol mixture with refractive index of 1.409. The 6 ns Q-switched Nd:YAG laser pulses of 532 nm wavelength are focused by a cylindrical lens to a ~100 μm×1 cm wide stripe aligned with the microfluidic channel. The fabrication and operation of the laser chip is fully compatible with silicone elastomer-based microfluidics technology [8].

When a $\pi/2$ phase-shifted DFB structure is used to provide the optical feedback, the lasing wavelength is determined by the Bragg condition:

$$m\lambda_m = 2n_{eff}\Lambda \tag{6.1}$$

where λ_m is the mth order resonant wavelength, n_{eff} is the effective index of the guided mode, and Λ is the grating period. Given Λ = 3080 nm and n_{eff} = 1.407, the 15th resonant wavelength and the free spectral range (*FSR*) are 577.8 nm and 41.3 nm respectively. This large *FSR* ensures that at most two resonances can simultaneously appear inside the gain spectrum (typically 30–50 nm wide for dye molecules). Thus single frequency operation is obtained even at high pump levels due to gain discrimination. Figure 6.2 shows the simulated reflectivity spectrum of the overall structure using the Rouard's method [9]. The parameters used are: Λ = 1280 nm + 1800 nm, grating length L = 1 cm, effective $\pi/2$ phase shift at the center, core index n_{core} = 1.409, and cladding/post index n_{clad} = 1.406. Also shown are the normalized measured fluorescence spectra of Rh6G and Rh101 solutions used in the lasing experiment.

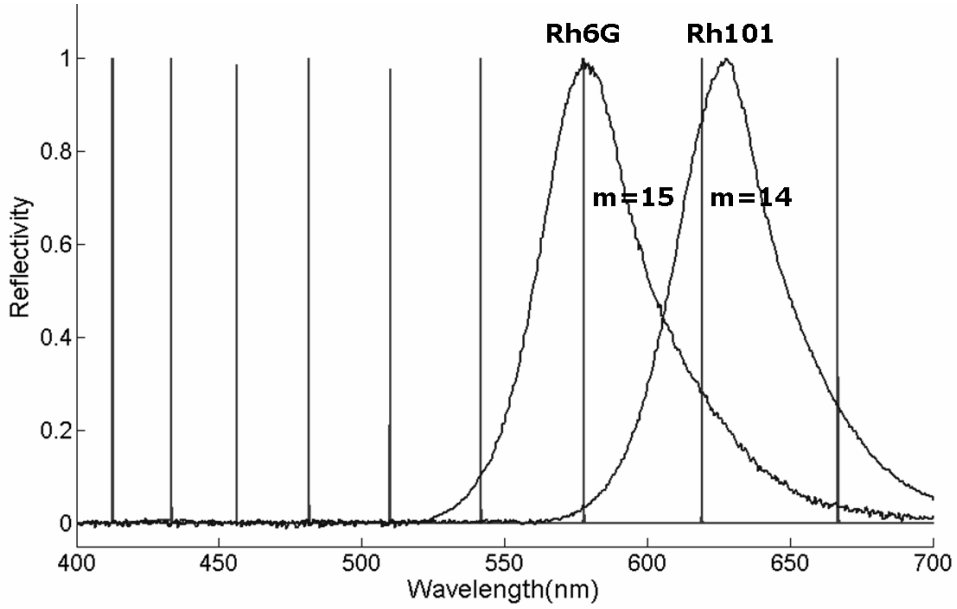

Figure 6.2. Simulated reflectivity spectrum of a $\pi/2$ phase-shifted higher-order DFB structure. The parameters used are given in the main text. Also shown are the normalized measured fluorescence spectra of Rh6G and Rh101 solutions used in the lasing experiment.

6.3 Wavelength tuning

The lasing wavelength can be tuned by changing either n_{eff}, Λ, or m, as has been demonstrated in conventional DFB dye lasers [10]. The effective index n_{eff} can be varied by changing the core index or the cross-sectional dimensions of the waveguide. However, due to the low Young's modulus of PDMS (~ 750 kPa) [11], the more straightforward tuning method is to change the grating period by simply stretching or compressing the chip along the waveguide direction. Finally, the grating order m can be chosen by using different dye molecules whose emission spectra cover different spectral regions. The last two methods were used in this work to achieve a nearly 60 nm tuning range from yellow to red. As can be seen from Figure 6.2, the potential tuning range for Rh6G and Rh101 is larger than 100 nm covering from 550 nm to beyond 650 nm. Actually, because of the multiple spectral

resonances supported by the higher order grating, this laser can provide tunable output covering the whole available dye laser spectrum from 320 nm to 1200 nm [12] when suitable dye molecules and pump light are used. With a mixture of several dye molecules, simultaneous multiple color lasing from the same cavity is also possible.

6.4 Results and discussion

To achieve the mechanical tuning, the laser chip was glued to two separate stages with the laser region suspended in the middle as shown in Figure 6.1. One of the stages is a high resolution micrometer with 1 μm sensitivity which provides accurate control and quantitative measurement of the deformation of the chip. This allows us to both stretch and compress the chip along the channel direction. The result of mechanical tuning is given in Figure 6.3. The points on the figure are experimental data and the curves are the linear fit. The achieved single mode tuning range for Rh6G is from 565 nm to 594 nm and is from 613 nm to 638 nm for Rh101. When the length of the central suspended region is 1cm, the total chip deformations required to achieve the above tuning ranges are about 500 μm for Rh6G and 400 μm for Rh101, which correspond to 28 nm and 25 nm grating period changes respectively. Because of the extremely large allowed deformation of PDMS (> 120%), the ultimate tuning range is limited by the gain bandwidth. Only ~ 5% deformation was used to achieve the ~60 nm tuning range. We believe an even wider tuning range from 550 nm to 650 nm is obtainable with a better cavity design and a more uniform mechanical load. The tuning is continuous and completely reversible due to the elastomer nature of PDMS. No noticeable degradation of the chip was observed during a 5-cycle full range tuning test. Throughout the tuning range, stable single-mode

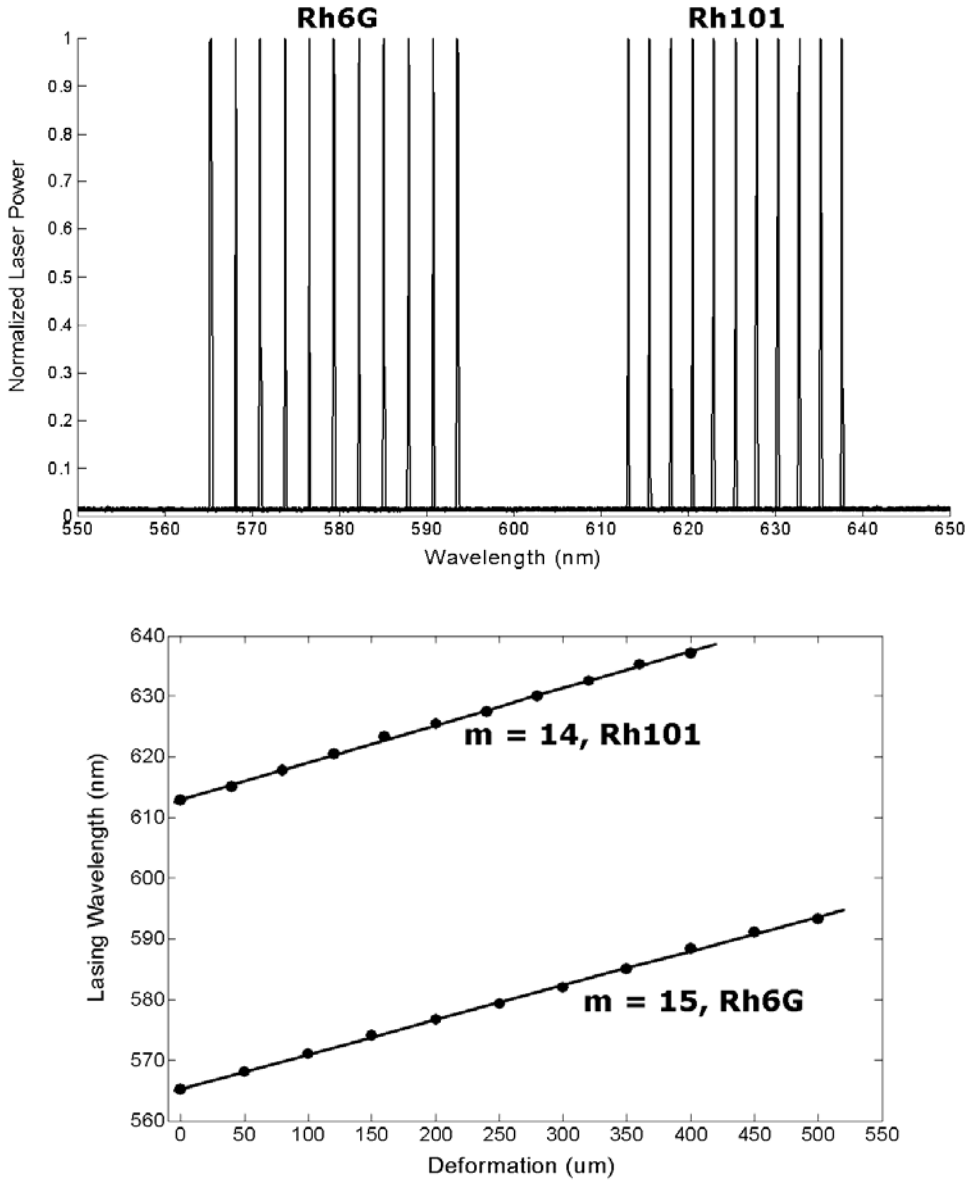

Figure 6.3. Upper: Normalized laser output of the mechanically tunable optofluidic DFB dye laser. Different peaks correspond to different grating periods. The measured laser linewidth is less than 0.1 nm throughout the tuning range. Lower: Lasing wavelength vs. the measured chip deformation. The points are the experimental data and the curve is the linear fit. The achieved single-mode tuning range for Rh6G is from 565 nm to 594 nm and is from 613 nm to 638 nm for Rh101.

operation was maintained with measured linewidth < 0.1 nm, resolution limited by the spectrometer (Ocean Optics HR4000). The absorbed pump thresholds are ~ 150 nJ and ~

200 nJ for Rh6G and Rh101, respectively. As expected, we observed the decrease of laser output power as the lasing wavelength moved away from the gain spectrum peak in either direction. The deformation along the channel causes its transverse dimensions to change also, which changes the effective index of the guided mode. However, given that the Poisson's ratio of PDMS is ~ 0.5, the estimated effective index change is only about 1.5×10^{-5} and its effect on the lasing wavelength is negligible.

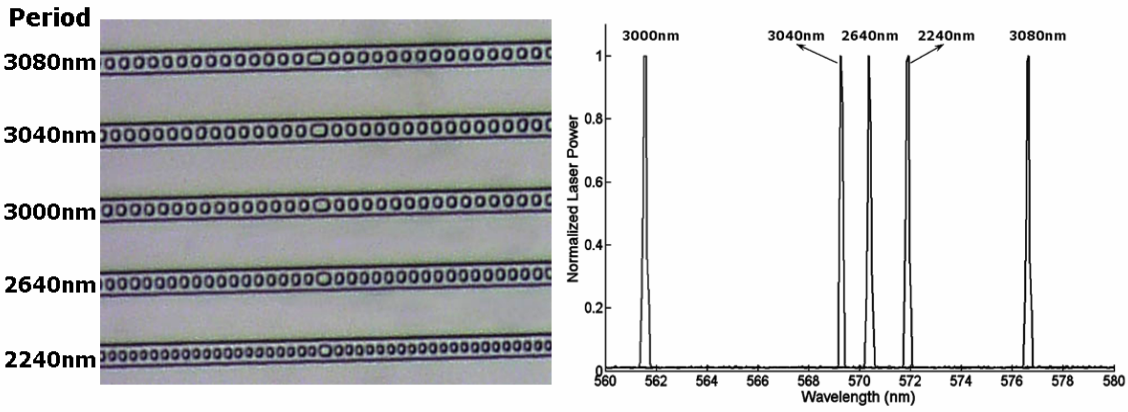

Figure 6.4. Left: Optical micrograph of an integrated array of five optofluidic DFB dye lasers. The grating period of each laser is given on the left. Right: Normalized laser output of the array using Rh6G dye solution as the gain medium

We also fabricated an array of five DFB dye lasers on a single PDMS chip. Figure 6.4 shows the lasing results using the Rh6G dye solution. Laser output spanning a ~ 15 nm range was achieved with different grating periods. The low pump threshold (< 1 uJ) of each optofluidic DFB dye laser makes it possible to use a single high energy pulsed laser to pump hundreds of such lasers on a chip. This opens up the possibility of building highly parallel multiplexed biosensors on a chip, such as multiple-color flow cytometers and surface plasmon resonance based sensors. This also provides an alternative to tunable

lasers for making compact and inexpensive wavelength scanning-less spectrometers on a chip [13].

6.5 Conclusion

We have demonstrated a continuously tunable optofluidic DFB dye laser on a monolithic PDMS chip using a simple mechanical deformation method. Single-mode operation was maintained throughout the achieved ~ 60 nm tuning range. Due to the higher order of the DFB structure, a single laser is capable of generating tunable output covering from near UV to near IR spectral region when a UV pump light is used. An integrated array of such lasers was also demonstrated. Such laser arrays can be used to make highly parallel multiplexed biosensors and scanning-less spectrometers on a chip. Finally, we want to point out that these lasers are still not stand-alone devices, because both the gas pressure source for the microfluidic valves and the pump laser are outside the chip. The gas pressure source can be eliminated by using electrokinetically driven flows. However, an external pump light is necessary for all dye lasers. For portable devices, visible semiconductor lasers can be used as the pump source.

Bibliography

1. Helbo, B., A. Kristensen, and A. Menon, *A micro-cavity fluidic dye laser*. Journal of Micromechanics and Microengineering, 2003. **13**(2): p. 307-311.

2. Vezenov, D.V., et al., *A low-threshold, high-efficiency microfluidic waveguide laser*. Journal of the American Chemical Society, 2005. **127**(25): p. 8952-8953.
3. Galas, J.C., et al., *Microfluidic tunable dye laser with integrated mixer and ring resonator*. Applied Physics Letters, 2005. **86**(26).
4. Bilenberg, B., et al. *Tunable microfluidic dye laser*. 2003.
5. Psaltis, D., S.R. Quake, and C.H. Yang, *Developing optofluidic technology through the fusion of microfluidics and optics*. Nature, 2006. **442**(7101): p. 381-386.
6. Li, Z.Y., et al., *Single mode optofluidic distributed feedback dye laser*. Optics Express, 2006. **14**(2): p. 696-701.
7. Yariv, A. and A. Yariv, *Optical electronics in modern communications*. 5th ed. Oxford series in electrical and computer engineering. 1997, New York: Oxford University Press. xviii, 744 p.
8. Unger, M.A., et al., *Monolithic microfabricated valves and pumps by multilayer soft lithography*. Science, 2000. **288**(5463): p. 113-116.
9. Wellerbrophy, L.A. and D.G. Hall, *ANALYSIS OF WAVE-GUIDE GRATINGS - APPLICATION OF ROUARD METHOD*. Journal of the Optical Society of America a-Optics Image Science and Vision, 1985. **2**(6): p. 863-871.
10. Shank, C.V., Bjorkhol.Je, and H. Kogelnik, *TUNABLE DISTRIBUTED-FEEDBACK DYE LASER*. Applied Physics Letters, 1971. **18**(9): p. 395-&.
11. McDonald, J.C. and G.M. Whitesides, *Poly(dimethylsiloxane) as a material for fabricating microfluidic devices*. Accounts of Chemical Research, 2002. **35**(7): p. 491-499.
12. Silfvast, W.T., *Laser fundamentals*. 2nd ed. 2004, Cambridge, UK ; New York: Cambridge University Press. xxiv, 642 p.
13. Oki, Y., et al., *Multiwavelength distributed-feedback dye laser array and its application to spectroscopy*. Optics Letters, 2002. **27**(14): p. 1220-1222.

Chapter 7

NANOIMPRINTED CIRCULAR GRATING DISTRIBUTED FEEDBACK DYE LASER

7.1 Introduction

In recent years, polymer dye lasers have attracted much attention due to their low-cost processing, wide choice of emission wavelengths, and easy fabrication on flexible substrates. Several waveguide dye lasers have been studied with emission wavelengths ranging from the ultraviolet to the near-infrared [1, 2]. By simply changing the fluorophore doped in the polymer these lasers can be used as the tunable sources for various applications, including spectroscopy [3]. The one dimentional (1-D) distributed feedback (DFB) resonator structure is widely employed and has been previously demonstrated for polymer lasers [4]. Operating characteristics can be significantly improved within two-dimensional structures. Here, a circular grating distributed feedback structure was used to obtain low threshold operation, a well-defined output beam, and vertical emission perpendicular to the device plane. Although surface emitting circular grating lasers using semiconducting polymers have been previously demonstrated by Bauer et al. [5] and Turnbull et al. [6, 7], their lasers were fabricated by depositing the organic gain material onto pre-patterned dielectric substrates, limiting the depth and the accuracy of the shape of the grating. To enable the mass production, the nanoimprint lithography [8] was chosen as a direct patterning method. A hard mold is used to transfer patterns with high fidelity into target polymers, and this technique has become an attractive approach to define

nanofabricated optical resonator structures. Conjugated polymer lasers fabricated by hot embossing have been studied by Lawrence et al. [9], and 1-D DFB lasers based on organic oligomers using a room-temperature nanoimprint method were reported by Pisignano et al. [10].

In this chapter, we report a circular grating distributed feedback laser fabricated within a dye-doped poly(methylmethacrylate) (PMMA) film on a glass substrate. The laser circular grating structure was fabricated using a low-cost and manufacturable nanoimprint method. Lasing with single mode surface emission at 618.52 nm and a linewidth of 0.18 nm was measured from the polymer dye laser exhibiting a threshold value of 1.31 nJ/mm^2. The laser operation characteristics of the circular grating resonator are improved through the high accuracy and aspect ratio nanoimprint pattern transfer. Moreover, the mold can be re-used repeatedly, providing a convenient mean of mass production and large scale fabrication of low cost polymer dye laser arrays.

7.2 Chip design and fabrication

The circular grating structure proposed by Erdogan and Hall [11] provides a natural two-dimensional extension of the basic DFB structure. It allows feedback to be applied in all in-plane directions, and the second-order grating couples the emitted radiation perpendicularly out of the surface of the sample. Figure 7.1 shows a general design of a circular grating distributed feedback structure. A theoretical analysis of circular grating is described in detail elsewhere [5, 12-14] predicting that only the radial propagating components define the modes in the circularly symmetric grating. The design parameters of the circular gratings fabricated for this chapter are selected based on electromagnetic mode calculations

and experimental results. A grating period of 440 nm is chosen to match the second order Bragg condition. The center defect is a 440 nm diameter gain region. The 400 nm groove

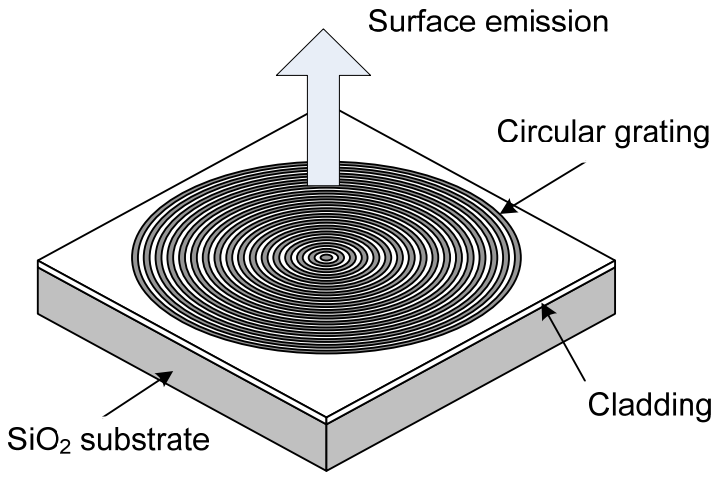

Figure 7.1. General design of a circular grating distributed feedback structure.

depth is defined to ensure maximum confinement, whereas the 200 μm overall diameter of the circular grating and the 50% duty cycle are used to reach the maximum coupling strength [6]. In our experiments, silicon dioxide (SiO_2) was used as the mold material and the grating pattern was defined by electron beam lithography on a LEICA EBPG 5000+ electron beam writer with proximity correction. The pattern was subsequently transferred into a SiO_2 substrate via reactive ion etching using CHF_3 plasma. PMMA was selected as the polymer matrix because of the solubility of the dye in PMMA, as well as its low optical absorption within the wavelength range for activating the dye molecules, and its excellent properties for nanoimprint lithography [15].

To construct the dye laser, a glass substrate was spin-coated with 5 μm of Cytop, a low refractive index material (n=1.34, Asahi Glass) as the lower cladding to ensure the vertical

optical confinement. Then, 500 nm Dye(Rhodamine 640, Exciton)-doped PMMA (30 mM) with the refractive index about 1.48 at emission wavelength was spin-coated on top of the Cytop layer as the gain medium. An oxygen plasma treatment (Anatech SP100) of the Cytop was necessary for good adhesion of Cytop to the PMMA.

Nanoimprint lithography exploits the glass transition of polymers to achieve high-fidelity pattern transfer. In order to reduce the degradation of photoluminesence efficiency of the organic materials at high temperatures during the nanoimprint lithography, a vacuum environment nanoimprint was demonstrated to have less than 5% reduction of degradation [16]. In our experiment, a simple alternative was used to reduce the degradation by sealing the imprinting mold and the PMMA substrate into an elastic PDMS mold during the imprinting process. This elastic mold serves as pressure balancing to reduce the inhomogeneous pressure due to the non-parallel presser heads. A mold release agent (surfactant) such as 1H,1H,2H,2H-perfluorodecyl-trichlorosilane (Alfa Aesar) was also deposited on the PMMA to reduce the resist adhesion to the mold. Then, the mold was pressed into the PMMA film by using an automatic mounting press machine (Buehler SimpliMet 1000) at a temperature of 150°C (above PMMA's glass transition temperature) and a pressure of 1200 psi. After sample cooling, the mold could be easily separated from the patterned polymer laser chip. The fabrication process is schematized in Figure 7.2.

Figure 7.3 shows SEM images of the mold and the imprinted PMMA. From these pictures, we can observe that the structure on the SiO_2 mold is faithfully replicated on the PMMA substrate surface with high resolution. The resolution of the nanoimprint could be as high

as sub 10 nm. Photoluminescence spectra confirm that there is no degradation of the luminescence performance of the polymer.

7.3 Measurement and laser characteristics

The polymer laser cavity was optically pumped with 6 nanosecond Q-switched Nd:YAG

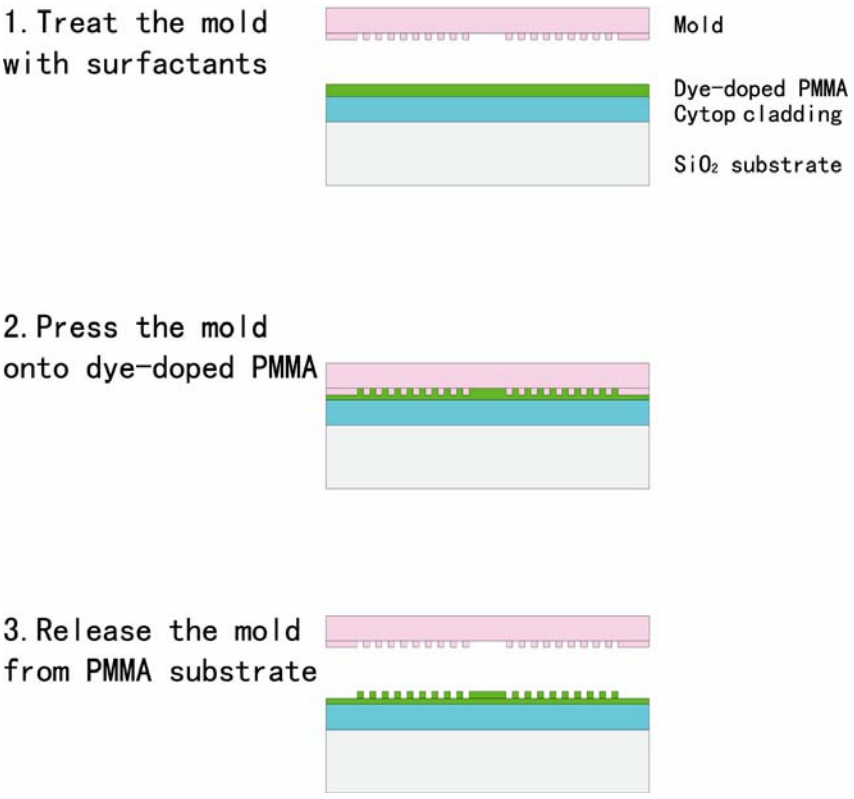

Figure 7.2. Schematic fabrication process of circular grating polymer dye laser

laser pulses at 532 nm wavelength, focused through a 20X objective to the back side of the chip. A 10X microscope objective was used to collect the emission from the top surface of the chip and deliver it to a fiber coupled CCD-array based spectrometer with 0.1 nm resolution (Ocean Optics HR4000). A typical single mode lasing spectrum is shown in

Figure 7.4. The lasing wavelength is 618.52 nm, and the measured linewidth is 0.18 nm.

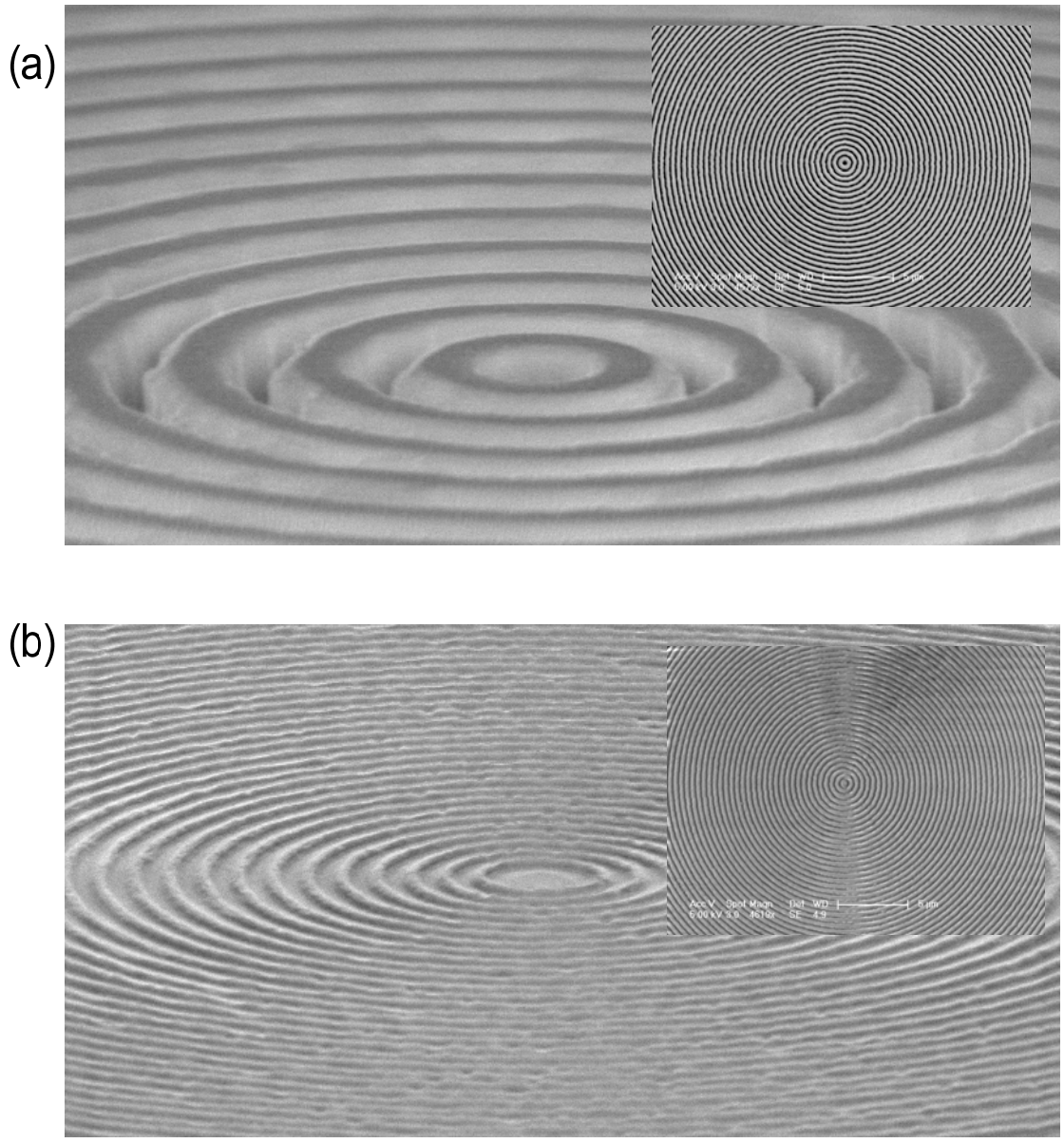

Figure 7.3 SEM images of angled view of (a) the SiO_2 mold and (b) the imprinted PMMA film with circular grating structure with top view of insets.

Lasing occurs near the Bragg resonance, determined by the equation $m\lambda_{Bragg} = 2n_{eff}\Lambda$, where m=2 is the order of diffraction, n_{eff} is the effective refractive index of the propagation mode, and Λ is the grating period. The lasers exhibit single mode emission, as

higher order modes do not appear, due to the smaller overlap between the mode profile and the gain region. The linewidth near threshold is measured as 0.20 nm, which results in a cavity quality factor (Q) of over 3000. The left inset of Figure 7.4 shows the variation of the output laser power as a function of the absorbed pump pulse fluence, and a laser threshold pump fluence of 1.31 nJ/mm^2 is observed. The absorbed pump pulse fluence was calculated

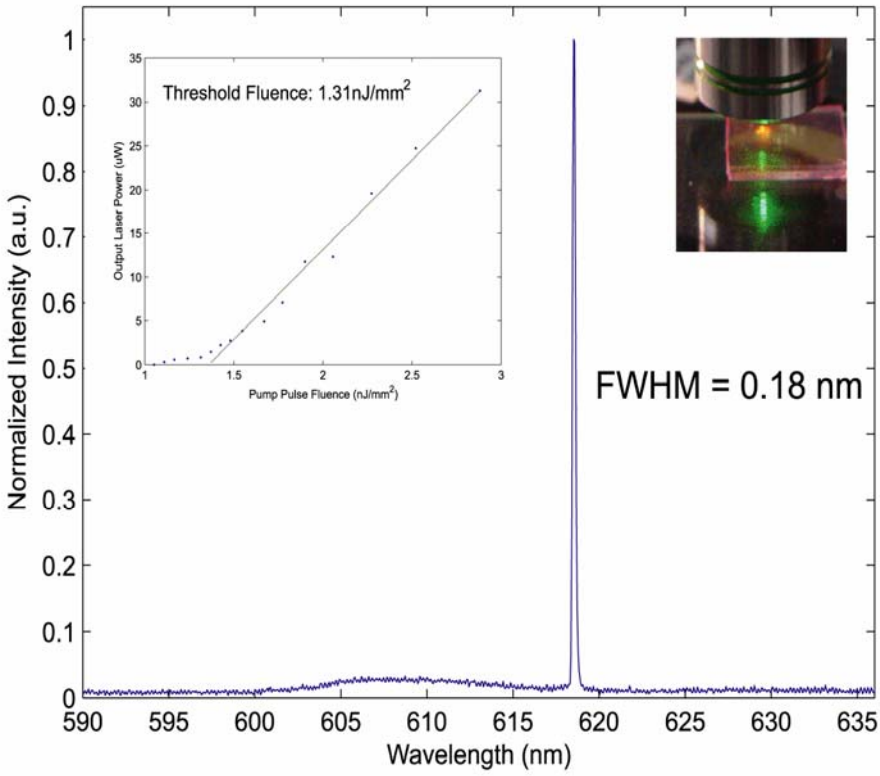

Figure 7.4. The typical nanoimprinted circular grating DFB dye laser spectrum. The measured linewidth is 0.18nm. Left inset: The pump laser pulse fluence vs. the absorbed pump pulse fluence. The threshold fluence is determined as 1.31 nJ/mm^2. Right inset: Polymer laser chip excited by Nd:YAG 532 nm laser pulses

with the pump pulse energy measured divided by the focal point which is about 600 μm in diameter and the output laser power was measured directly using the power meter. This

pump intensity is well within the reach of commercial high power blue laser diodes (LDs), enabling a self-contained LD pumped device. The right inset of Figure 7.4 shows that the polymer laser is pumped from the back side and the lasing emission is collected from the surface of the chip. The transparency of the substrate, the size and geometry of the laser cavity and the low threshold also match well with the output beams of high power LEDs and LDs. Therefore the replication-molded ring geometry represents a very promising structure for the construction of compact LED or LD pumped portable dye lasers.

We observe decreases in the laser emission with increasing exposure time. This result is consistent with previous studies on polymer DFB structures [17]. The lifetime of polymer dye laser can last over 10^6 shots (of pump laser pulses), and if the characterization of the device is carried out under vacuum to inhibit photo-oxidation, the lifetime can be further extended [18]. Because of the low cost of materials and fabrication, replication molded devices are disposable and may not require a long lifetime. In the future, we plan to make an optofluidic version [4] of the circular grating dye laser which allows us to constantly change the dye to increase the device lifetime and to tune the wavelength.

7.4 Conclusion

In summary, we demonstrated a surface emitting polymer dye laser with a circular grating distributed feedback structure realized by nanoimprint lithography. We achieved excitation thresholds as low as 1.31 nJ/mm^2 and FWHM linewidths of 0.18 nm. The technique described here enables the fabrication of low-cost, high-quality and mass-producible laser arrays, which may be deployed as compact and inexpensive coherent light sources for lab-on-a-chip applications such as sensing and spectroscopy. The two weakness of this

structure are: low vertical optical confinement (low refractive contrast) so the threshold would be reduced mainly through the increasing of the gain of the gain medium; degradation of the dye emission efficiency during the operation. The first weakness could be improved by using high index contrast design, and the second could be avoided by the dye circulation. The ultimate goal is to reduce the lasing threshold to enable the use of LEDs or LDs pumping as integrated and inexpensive pump sources for on-chip polymer lasers with wavelength tunability through different mechanisms which include mechanical tuning, temperature fine tune, and tuning by circulating different dyes.

Bibliography

1. Oki, Y., et al., *Fabrication of a distributed-feedback dye laser with a grating structure in its plastic waveguide.* Applied Optics, 2002. **41**(24): 5030-5035.
2. Oki, Y., et al., *Wide-wavelength-range operation of a distributed-feedback dye laser with a plastic waveguide.* Japanese Journal of Applied Physics Part 1-Regular Papers Short Notes & Review Papers, 2002. **41**(11A): 6370-6374.
3. Oki, Y., et al., *Multiwavelength distributed-feedback dye laser array and its application to spectroscopy.* Optics Letters, 2002. **27**(14): 1220-1222.
4. Li, Z.Y., et al., *Single mode optofluidic distributed feedback dye laser.* Optics Express, 2006. **14**(2): 696-701.
5. Bauer, C., et al., *A surface-emitting circular grating polymer laser.* Advanced Materials, 2001. **13**(15): 1161.

6. Turnbull, G.A., et al., *Effect of gain localization in circular-grating distributed feedback lasers.* Applied Physics Letters, 2005. **87**(20)
7. Turnbull, G.A., et al., *Influence of grating characteristics on the operation of circular-grating distributed-feedback polymer lasers.* Journal of Applied Physics, 2005. **98**(2)
8. Chou, S.Y., P.R. Krauss, and P.J. Renstrom, *Nanoimprint lithography.* Journal of Vacuum Science & Technology B, 1996. **14**(6): 4129-4133.
9. Lawrence, J.R., et al., *Optical properties of a light-emitting polymer directly patterned by soft lithography.* Applied Physics Letters, 2002. **81**(11): 1955-1957.
10. Pisignano, D., et al., *Oligomer-based organic distributed feedback lasers by room-temperature nanoimprint lithography.* Applied Physics Letters, 2003. **83**(13): 2545-2547.
11. Erdogan, T. and D.G. Hall, *Circularly Symmetrical Distributed Feedback Semiconductor-Laser - an Analysis.* Journal of Applied Physics, 1990. **68**(4): 1435-1444.
12. Greene, P.L. and D.G. Hall, *Effects of radiation on circular-grating DFB lasers - Part I: Coupled-mode equations.* IEEE Journal of Quantum Electronics, 2001. **37**(3): 353-364.
13. Greene, P.L. and D.G. Hall, *Effects of radiation on circular-grating DFB lasers - Part II: Device and pump-beam parameters.* IEEE Journal of Quantum Electronics, 2001. **37**(3): 365-371.
14. Barlow, G.F., et al., *Design and analysis of a low-threshold polymer circular-grating distributed-feedback laser.* Journal of the Optical Society of America B-Optical Physics, 2004. **21**(12): 2142-2150.
15. Chou, S.Y., P.R. Krauss, and P.J. Renstrom, *Imprint of Sub-25 Nm Vias and Trenches in Polymers.* Applied Physics Letters, 1995. **67**(21): 3114-3116.
16. Wang, J., et al., *Direct nanoimprint of submicron organic light-emitting structures.* Applied Physics Letters, 1999. **75**(18): 2767-2769.
17. Heliotis, G., et al., *Two-dimensional distributed feedback lasers using a broadband, red polyfluorene gain medium.* Journal of Applied Physics, 2004. **96**(12): 6959-6965.
18. Del Carro, P., et al., *Near-infrared imprinted distributed feedback lasers.* Applied Physics Letters, 2006. **89**(20)

Chapter 8

MASK PATTERN TRANSFERRED TRANSIENT GRATING TECHNIQUE FOR MOLECULAR-DYNAMICS STUDY IN SOLUTIONS

8.1 Introduction

The transient grating (TG) technique [1, 2], which is one of the third-order nonlinear spectroscopies, has been a powerful tool to monitor several photonics and photochemical processes in solutions since its outset. For a brief history, solutions were photoexcited by an optical interference pattern generated by two crossing pump beams. As parameters, several properties of a solution were spatially modulated according to the interference pattern and were detected through the diffraction of the probe beam. The time-varying profiles of the diffracted signal indicate the many processes in solution, such as electron transfer, molecular dynamics, heat dynamics, ultrasonics, volume/structure change, clustering/aggregation, and chemical reaction [3-8]. The optical heterodyne detected-TG (OHD-TG) technique [9-16] was also developed later to improve sensitivity. The reference beam, which has the same direction, polarization, and wavelength as the signal beam, was superimposed on the signal beam to amplify the signal intensity. The experimental setups of the OHD-TG were very difficult because the probe and reference beams need to be aligned and tuned within submicron meter scale to meet the phase-matching condition. Very recently, Katayama et al. developed a lens-free OHD-TG technique [17, 18] by using a transmission grating structure in a 3 mm glass. This technique was easier than the traditional OHD-TG technique. In this chapter, we describe a more convenient and easy

well aligned technique; the mask pattern transferred—TG (MPT-TG) technique—by using a metal film grating fabricated in our laboratory.

8.2 Experimental setup

Figure 8.1a shows the scanning electron microscope (SEM) image of the smallest metal grating film (400 nm metal width and 1 μm period). Chromium layer (100 nm) was created by vacuum evaporation on the quartz substrate. A fine grade resist was deposited on a Cr layer by spin coating. Nano or micrometer scaled patterns are written by the lithography

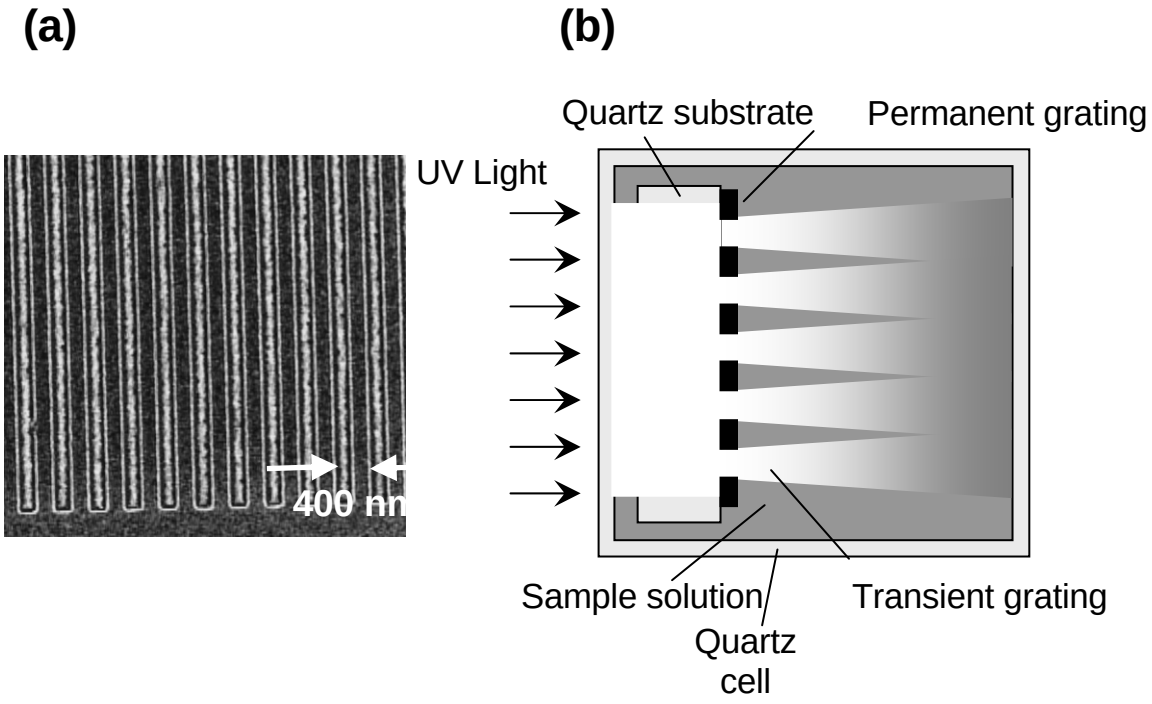

Figure 8.1 (a) Scanning electron microscope (SEM) image of the smallest fabricated nano metal grating. (b) Schematic diagram of the pattern transfer from the metal grating film to the solution

of an electron beam or a direct writing laser. Finally, metal grating structures are engraved by chemical etching. The principle of the MPT-TG is depicted in Figure 8.1b. A finished metal grating film is suspended into the sample solution and the excitation UV pump beam

(I_e) is incident at the grating in solution. Thus the grating pattern is transferred from the metal film to the sample solution under near-field condition (Fresnel diffraction). This is similar to traditional photo-lithography but, in this case, the sample material is liquid solution. The solute molecules were excited by this special transient grating (TG) structure. A part of the probe beam (I_p) irradiated on the grating in the solution is diffracted under the far-field condition (Fraunhoffer diffraction) and was detected by the photodetector.

The experimental setup of the MGT-TG is schematically shown in Figure 8.2. A

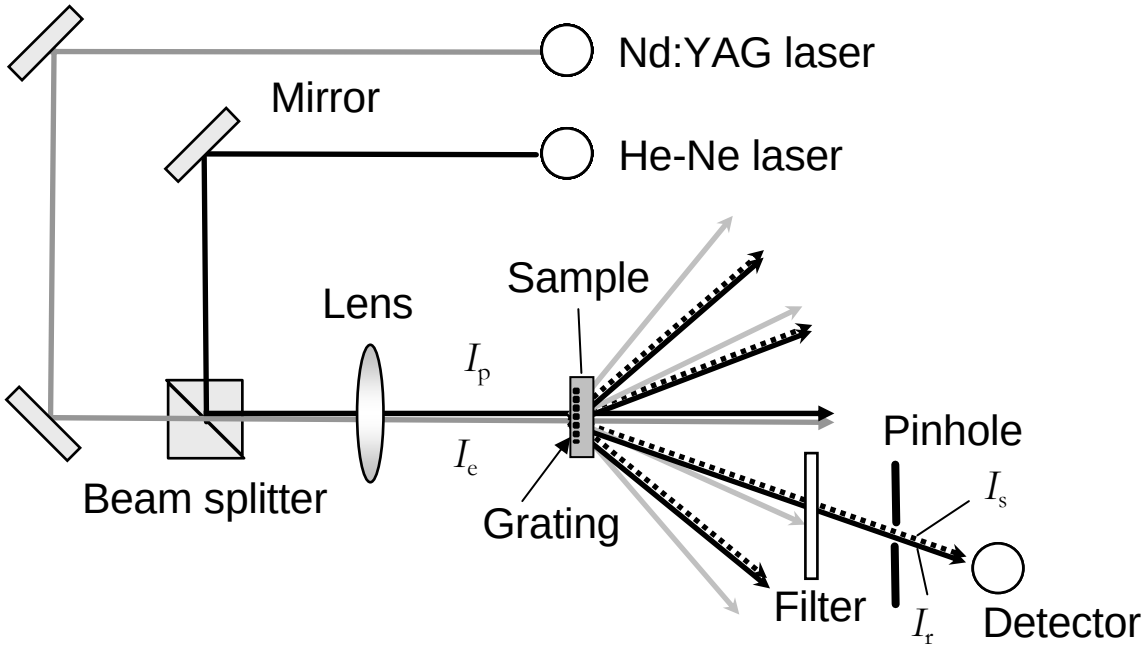

Figure 8.2 Experimental setup of the MPT-TG technique with metal grating and the optical configurations of irradiated pump (I_e) and probe (I_p) beams and diffracted reference (I_r) and signal (I_s) beams

frequency-tripled Nd:YAG laser (λ_e = 366 nm, I_e = 0.3 mJ/pulse) was used as a pump beam. The pulse width and repetition rate are 10 ns and 3 Hz, respectively. A cw-He-Ne laser (λ_p = 633 nm, I_p = 0.05 mW) is used as a probe beam. Both beams are focused by a lens on the

sample solution in a quartz cell (10 mm spacing). A limited diffraction beam passes through a pinhole and a glass filter and is registered with an InGaAs photodetector. Two types of signals, diffracted by permanent metal grating (I_r) and transient grating (I_s), are simultaneously detectable. The permanent grating signal plays the role of the reference beam of the OHD-TG setup and amplifies the transient grating signal. Both diffracted signals pass the color filter and pinhole to be separated from the pump beam and detected onto the photodetector.

Sample solution was nitrobenzene in 2-propanol (5 volume %). The excited energy of nitrobenzene is immediately converted to molecular vibration, translation, and finally heat energy. Such non-radiative relaxation processes of nitrobenzene are completed within a very short time-scale (a few hundred picoseconds) [19]. Therefore, nitrobenzene has been used often as the standard solution of the typical heat source (molecular heater) for photothermal measurement.

8.3 Results and discussion

Figure 8.3 shows the semi-log plot of the time-dependent diffraction signals with (a) micron-meter scaled and (b) nano-meter scaled etch width metal grating, respectively. We found the exponential decay component (I_s) superimposed on the large non-decayed offset component (I_r). The former is due to the transient grating while the latter is due to the permanent grating, respectively. According to the theory, detected total signal intensity (I_{total}) can be described by [17, 18]

$$I_{total}(t) = I_r + 2a\left[\chi^{(3)}{}'(t)\cos\Delta\phi + \chi^{(3)}{}''(t)\sin\Delta\phi\right]I_e I_p + \left|\chi^{(3)}(t)\right|^2 I_e{}^2 I_p \qquad (8.1)$$

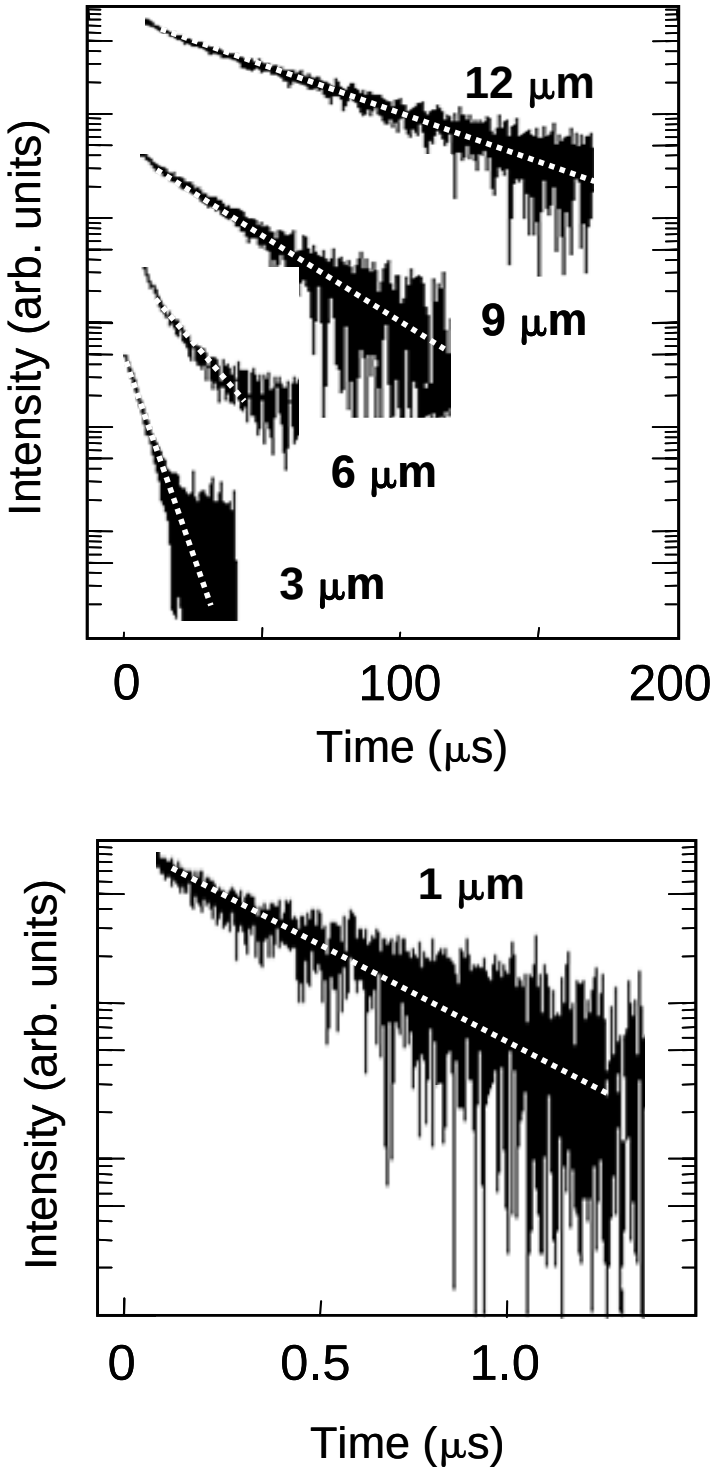

Figure 8.3 Time profile of the diffracted signals with metal grating of 12, 9, 6, and 3 μm periods (a) and 1 μm period (b). Dashed lines were fitted by the exponential functions.

where $\chi^{(3)}$'(t) and $\chi^{(3)}$"(t) are the real part and imaginary part, respectively, of the third-order nonlinear electrical susceptibility $\chi^{(3)}$ (t), and a is a real constant. The third term indicates the TG signal with usual homodyne detection and is negligible because involved $\chi^{(3)}$ in solution should be very small. Thus, only the second term of equation (8.1) indicates I_s. In this case, $\chi^{(3)}$'(t) and $\chi^{(3)}$"(t) are equal to the refractive index change $\delta n(t)$ and the absorbance change $\delta k(t)$=0 at 633 nm induced by the transient grating, respectively. $\Delta\phi$ is the phase difference between I_r and I_p. In the OHD-TG techniques, unstable $\Delta\phi$ has been the main difficulty of the experimental setup. However, in our setup, $\Delta\phi$ is decided only by the structure and thickness of the metal grating. Therefore, the phase stability is excellent without the tuning of beam lines in this setup. Thus, sin$\Delta\phi$ in equation (8.1) should be a constant, and I_s should be proportional to $\delta n(t)$.

The spatial modulation of the optical intensity (δI_e) induced the spatial modulation of the population of the molecular excited states (δP), temperature (δT), and density of solvent ($\delta\rho$). Namely, δn should be attributed to δT and $\delta\rho$ in this time scale. Temperature rising increases $\delta\rho$, which decreases δn. Therefore, spatial distribution of temperature (thermal grating) was created, and the signal decay shows the thermal diffusion processes in solution. By solving the Fourier's diffusion equation, the time profile of $\delta n(t)$ is given by [20]

$$\delta\hat{n}(t) = \left[\left(\frac{\partial n}{\partial \rho}\right)_T \left(\frac{\partial \rho}{\partial T}\right) + \left(\frac{\partial n}{\partial T}\right)_\rho\right] \frac{Q}{\rho C_p} \delta I_e [C] \exp(-D_{th} q^2 t) \tag{8.2}$$

where, Q, C_p, and [C] are the heat energy released from unit molecules, specific heat capacity, and solute molecular concentration. $\delta\hat{n}(t)$ is the spatial Fourier component of

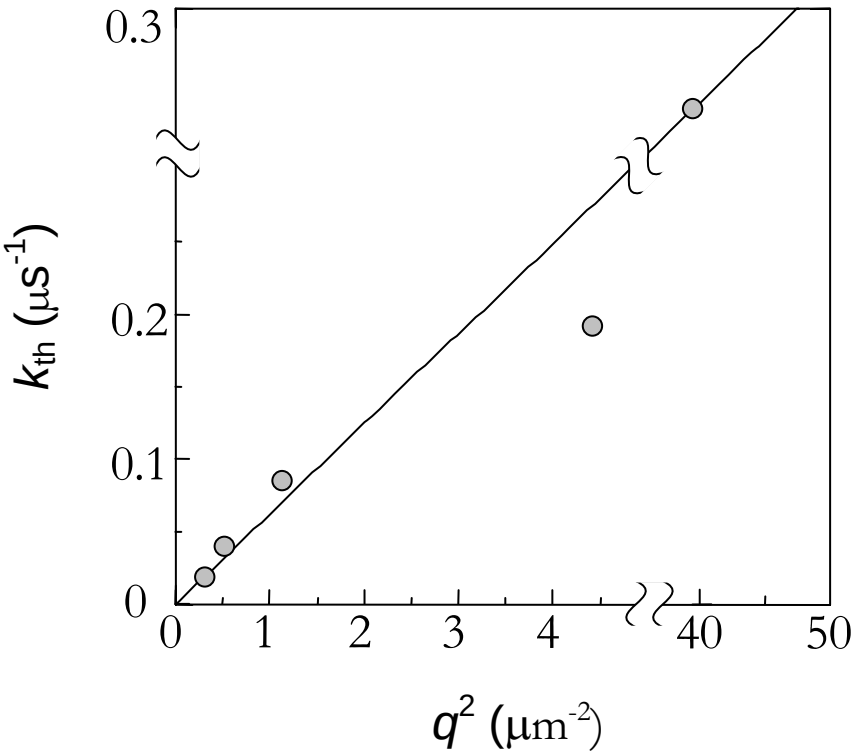

Figure 8.4 Relationship between the square of the grating constants (q^2) and the decay rate (k_{th}) of the TG signals. This slope indicates the thermal diffusion coefficient.

$\delta n(t)$. q is the grating constant described by the grating period (Λ) as $q=2\pi/\Lambda$. D_{th} is the thermal diffusion coefficient of solution. Therefore, signal decay rate ($k_{th}=1/\tau$) obtained by the exponential fitting was described by $k_{th}= D_{th}\ q^2$. Figure 8.4 shows the relationship between k_{th} and q^2 at each grating period, where a good linear relationship and D_{th} value is shown by the slope. The obtained value ($D_{th} = 7.0 \pm 0.7 \times 10^8$ m^2s^{-1}) is very close to the calculated value ($D_{th} = 6.8 \times 10^8$ m^2s^{-1}) [18] by the thermal conductivity (κ) of 2-propanol as $D_{th} = \kappa/\rho C_p$. This agreement demonstrates the validity of this method according to signal analysis above. By the same token, several diffusion processes, such as the molecular

diffusion in solution, energy migration in materials, or the carrier diffusion in semiconductors, should be measurable.

The MPT-TG technique should have many merits for photonic and photochemical application. The experimental setup and the beam alignment of the MPT-TG are simpler and easier than those of the usual OHD-TG technique, while it has very high signal sensitivities and S/N ratios for the optical heterodyne detection. The pump and probe beam should be incident at the same spot on the metal grating film, but the tunings of direction and phase of the beams are not necessary. The lens-free OHD-TG technique [17, 18] has similar merits. But the MPT-TG technique has still more merits compared to the lens-free technique. In the lens-free technique, an optical interference pattern was constructed by the diffraction light with transmission grating on the sample located behind the grating. The phase differential $\Delta\phi$ can be controlled by the distance (~ 250 μm usually) between the grating and the sample. In the MPT-TG technique, metal film grating is suspended into the sample solution and the transient grating structure is created directly behind it. Thus, $\Delta\phi$ is decided only by the thickness of the metal layer and the incident angle. Therefore, $\Delta\phi$ stability is controllable by the thickness of the metal layer. Moreover, various patterns can be used flexibly with any metal widths and periods to optimize the sensitivity. The measurement of the grating periods dependence is also very easy to control by sliding the film to change the pattern structure.

8.4 Conclusion

In conclusion, our new technique by using nano or micro metal grating film has many advantages compared to the traditional techniques. This technique should be a powerful

and useful tool for wider applications in physics, chemistry, material, and biological applications.

Bibliography

1. Shen, Y.R., *The principles of nonlinear optics*. 1984, New York: J. Wiley. xii, 563 p.
2. Eichler, H.J., P. Günter, and D.W. Pohl, *Laser-induced dynamic gratings*. 1986, Berlin ; New York: Springer-Verlag. xi, 256 p.
3. Fayer, M.D., *Dynamics of Molecules in Condensed Phases - Picosecond Holographic Grating Experiments*. Annual Review of Physical Chemistry, 1982. **33**: p. 63-87.
4. Terazima, M., K. Okamoto, and N. Hirota, *Transient radical diffusion in photoinduced hydrogen abstraction reactions of benzophenone probed by the transient grating method*. Journal of Physical Chemistry, 1993. **97**(50): p. 13387-13393.
5. Dhar, L., J.A. Rogers, and K.A. Nelson, *Time-resolved vibrational spectroscopy in the impulsive limit*. Chemical Reviews, 1994. **94**(1): p. 157-193.
6. Rogers, J.A. and K.A. Nelson, *Study of lamb acoustic wave-guide modes in unsupported polyimide thin-films using real-time impulsive stimulated thermal scattering*. Journal of Applied Physics, 1994. **75**(3): p. 1534-1556.
7. Terazima, M., *Translational diffusion of intermediate species in solutions*. Research on Chemical Intermediates, 1997. **23**(9): p. 853-901.
8. Terazima, M., K. Hirai, and H. Tomioka, *Translational diffusion of chemically active species: carbenes and carbonyl oxides*. Chemical Physics Letters, 1998. **289**(3-4): p. 253-260.
9. Goodno, G.D., G. Dadusc, and R.J.D. Miller, *Ultrafast heterodyne-detected transient-grating spectroscopy using diffractive optics*. Journal of the Optical Society of America B-Optical Physics, 1998. **15**(6): p. 1791-1794.

10. Goodno, G.D. and R.J.D. Miller, *Femtosecond heterodyne-detected four-wave-mixing studies of deterministic protein motions. II. Theory and experimental technique of diffractive optics-based spectroscopy*. Journal of Physical Chemistry A, 1999. **103**(49): p. 10619-10629.

11. Terazima, M., *Optical heterodyne detected transient grating for studies of photochemical reactions and solution dynamics*. Chemical Physics Letters, 1999. **304**(5-6): p. 343-349.

12. Terazima, M., *Optical heterodyne detected transient grating for the separations of phase and amplitude gratings and of different chemical species*. Journal of Physical Chemistry A, 1999. **103**(37): p. 7401-7407.

13. Dadusc, G., et al., *Diffractive optics-based heterodyne-detected four-wave mixing signals of protein motion: From "protein quakes" to ligand escape for myoglobin*. Proceedings of the National Academy of Sciences of the United States of America, 2001. **98**(11): p. 6110-6115.

14. Torre, R., A. Taschin, and M. Sampoli, *Acoustic and relaxation processes in supercooled orthoterphenyl by optical-heterodyne transient grating experiment*. Physical Review E, 2001. **6406**(6).

15. Xu, Q.H., et al., *Wavelength-dependent resonant homodyne and heterodyne transient grating spectroscopy with a diffractive optics method: Solvent effect on the third-order signal*. Journal of Chemical Physics, 2002. **116**(21): p. 9333-9340.

16. Gedik, N., et al., *Diffusion of nonequilibrium quasi-particles in a cuprate superconductor*. Science, 2003. **300**(5624): p. 1410-1412.

17. Katayama, K., M. Yamaguchi, and T. Sawada, *Lens-free heterodyne detection for transient grating experiments*. Applied Physics Letters, 2003. **82**(17): p. 2775-2777.

18. Yamaguchi, M., K. Katayama, and T. Sawada, *Lens-free heterodyne transient grating method for dynamics measurement of photoexcited species in liquid*. Chemical Physics Letters, 2003. **377**(5-6): p. 589-594.

19. Yip, R.W., et al., *Picosecond excited-state absorption of alkyl nitrobenzenes in solution*. Journal of Physical Chemistry, 1984. **88**(24): p. 5770-5772.

20. Terazima, M., K. Okamoto, and N. Hirota, *Diffusion process of methyl red in organic-solvents studied by the transient grating method*. Journal of Physical Chemistry, 1993. **97**(19): p. 5188-5192.

Chapter 9

CONCLUSION AND FUTURE WORK

The research in this thesis presents fabrication and characterization of: visible sub micrometer disk lasers, visible photonic crystal slab lasers based on InGaP/InGaAlP quantum well material system; and mechanically tunable one dimensional DFB microfluidic dye lasers based on PDMS, nanoimprinted two dimensional circular grating dye lasers based PMMA. The ultra-small size of the submicron disk lasers are the smallest lasers in absolute size and the visible photonic crystal slab lasers have the smallest mode volume so far. Both are well suited for ultra-compact spectroscopic sources. The realization of two dye lasers based on the microfluidic technology enables the integration of optofluidic integrated devices.

There is still a great deal of further work to be done:

- Identify the optical mode within our ultra-small disk lasers

As described earlier, the mode observed might be the chaotic mode or higher order mode by the vertical free space pumping. We will try to use the fiber couple pumping to investigate if the whispering gallery mode would be pumped that way and to push the size limit further.

- Use the disk structure to study the surface plasmon

Our disk structure has the advantage of a thin disk membrane which could be used to enhance the surface plasmon. We will explore more how the surface plasmon would affect the laser characteristics.

- Modify the photonic crystal design for the spectroscopic source

By modifying the photonic crystal structure to have an air hole in the middle of the structure, we expect high field intensity was presented and that could be used for the spectroscopic source, as well as a high sensitivity refractive index monitor sensor. Before that, we would like to utilize the high Q toroid structure to start investigation.

- Electrically driven photonic crystal laser

The realization of the electrically pumped photonic crystal lasers are of great importance for being really functional miniaturized. We will try to explore different current injection paths and different types of PN junction. The high-frequency electrical signal would be used to test the speed of our ultra-small lasers. A polarization detector will be fabricated using the same structure.